

**Real-time 3D Robotic Path Planning
from a Single Fluoroscopic Image for
Fenestrated Endovascular Aortic
Repair**

Jian-Qing Zheng

A thesis submitted in partial fulfillment of the requirements for the degree of
M.Res. in Medical Robotics and Image Guided Intervention and for the Diploma of
Imperial College

IMPERIAL COLLEGE LONDON

THE HAMLYN CENTRE FOR ROBOTIC SURGERY

September 2018

Supervised by:
Prof. Guang-Zhong Yang,
Ms. Xiao-Yun Zhou

Acknowledgments

I would like to express my deep gratitude to my project supervisors Prof. Guang-Zhong Yang and Ms. Xiao-Yun Zhou for their invaluable supervision, guidance and support. I would also like to acknowledge the bursary from the Hamlyn Centre for Robotic Surgery, which is a precious support during this year.

I would like to thank Ms. Celia Theodoreli Riga for providing the clinical data and the background knowledge in the clinical practice, which are the basis of the experiments in this project.

I would like to offer my special thanks to my friends, Qing-Biao Li, for the kind assistance and encouragement, Harry Chang, for the language instruction, Davide Shi, for the delicious food, and also thank all the other people within the Hamlyn Centre, for their kindness and friendly assistance.

The last but not the least, I would like to express my great appreciate to my parents, for their understanding and supporting, both financially and spiritually.

Abbreviations

Acronym	Description
AAA	Abdominal Aortic Aneurysm
BFGS	Broyden - Fletcher - Goldfarb - Shanno
BFS	Breadth First Searching
CPU	Central Processing Unit
CT	Computer Tomography
DCNN	Deep Convolutional Neural Network
DSC	Dice Similarity Coefficient
FCN	Fully Convolutional Network
FEVAR	Fenestrated Endovascular Aortic Repair
GM	Graph Matching
GPU	Graphic Processing Unit
G.&T.	Gray value variation and Translation
ICP	Iterative Closest Point
IR	Inlier Ratio
I-Skeleton	Intra-operative Skeleton
NP-hard	Non-deterministic Polynomial acceptable
P-Skeleton	Pre-operative Skeleton
QAP	Quadratic Assignment Problem
RPN	Region Proposal Network
R-CNN	Region based Convolutional Neural Network
R.&M.	Rotation and Mirroring
TPS	Thin Plate Spline

Abstract

Fenestrated Endovascular Aortic Repair (FEVAR) is currently guided by 2D fluoroscopic images, providing insufficient anatomical information to surgeons. It increases the difficulty and duration of FEVAR, which raises the probability of complications and the radiation doses of both patients and surgeons. This research project is to achieve a real-time 3D robotic path planning from a single fluoroscopic image for real-time 3D FEVAR navigation, including three main steps, the Abdominal Aortic Aneurysm (AAA) segmentation from a Computer Tomography (CT) volume and a fluoroscopic image, the skeletonization of the segmented AAA shapes in 2D and 3D, and the non-rigid 2D/3D registration of the AAA skeletons. In the first step, the AAA was segmented using U-net to avoid the overfitting caused by a small number of training subjects. A deformable 2D/3D registration method of AAA skeletons based on graph matching was proposed in the third step. The graph of 2D and 3D skeletons were constructed, and the nodes of branches and trunks were searched and classified for 2D/3D correspondence of skeleton graphs. An energy function measuring the re-projected difference between 2D and 3D skeletons with constraints of length preservation and smoothness was optimized to achieve a deformed 3D skeleton. The 34-layer U-Net with the data augmentation of gray value variation and translation achieved a reasonable average Dice Similarity Coefficient result about 0.8. Evaluated with three criteria, the proposed method performed accurately and efficiently on the simulation, phantom and patient data with high robustness to the translation and rotation parallel to the projection plane, as well as the shape deformation. Hence, the 3D deformation recovering of an intra-operative AAA skeleton from a single fluoroscopic image was achieved potentially for the 3D robotic path planning in FEVAR. (12763 words)

Contents

1	Introduction	1
1.1	Background	2
1.2	Literature Review	4
1.2.1	2D Segmentation	4
1.2.2	2D/3D Registration	7
2	Methodology	11
2.1	Segmentation and Reconstruction	12
2.1.1	Data Augmentation	12
2.1.2	Network Architecture and Training	13
2.1.3	Post-processing and 3D Reconstruction	13
2.2	Skeleton Extraction	14
2.3	2D/3D Registration of Skeletons	14
2.3.1	Skeleton Graph Construction	16
2.3.2	Node Classification	19
2.3.3	Node Matching	23
2.3.4	Iterative Optimization for Deformation	28

2.3.5 Post-processing	32
2.4 Experiments and Validation	32
2.4.1 Validation for Segmentation and Reconstruction	32
2.4.2 Validation for Deformable Registration	33
3 Results	38
3.1 Segmentation and Reconstruction Results	38
3.2 Deformable Registration Results	40
3.2.1 Simulated Data Experiment	40
3.2.2 Phantom Data Experiment	46
3.2.3 Patient Data Experiment	49
4 Discussion	52
4.1 Performance Analysis	52
4.1.1 Accuracy	52
4.1.2 Runtime	54
4.1.3 Robustness	55
4.2 Achievement and Limitation	58
4.3 Future work	59
4.4 Conclusion	59
Bibliography	66
Appendix	67

Chapter 1

Introduction

This project is to research on the 3D deformation recovering of an abdominal aortic aneurysm (AAA) skeleton for the path planning of the surgery robot in fenestrated endovascular aortic repair (FEVAR). An accurate geometrical arrangement is required for the robotic implant placement of fenestrated stent-grafts assisted in FEVAR. At present, this process is navigated using 2D information from real-time fluoroscopic images, without illustrating the contours of aortas and arteries or providing 3D anatomical information to the surgeons. It leads to the loss of depth perception and lack of information. The development of a 3D deformation recovering of an AAA skeleton is thus necessary for FEVAR, in which a deformed 3D AAA skeleton is re-created from a single intra-operative 2D image of real-time fluoroscopy to provide a real-time 3D navigation for FEVAR. As shown in the fig. 1.1(b), the 3D path planning contains three principal procedures in this project, segmentation of the aneurysm tissue from a pre-operative computed tomography (CT) volume and an intra-operative fluoroscopic image from the same patient, skeletonization of the 2D/3D AAA shape, non-rigid registration of the 2D and 3D skeleton including rigid and deformable registration.

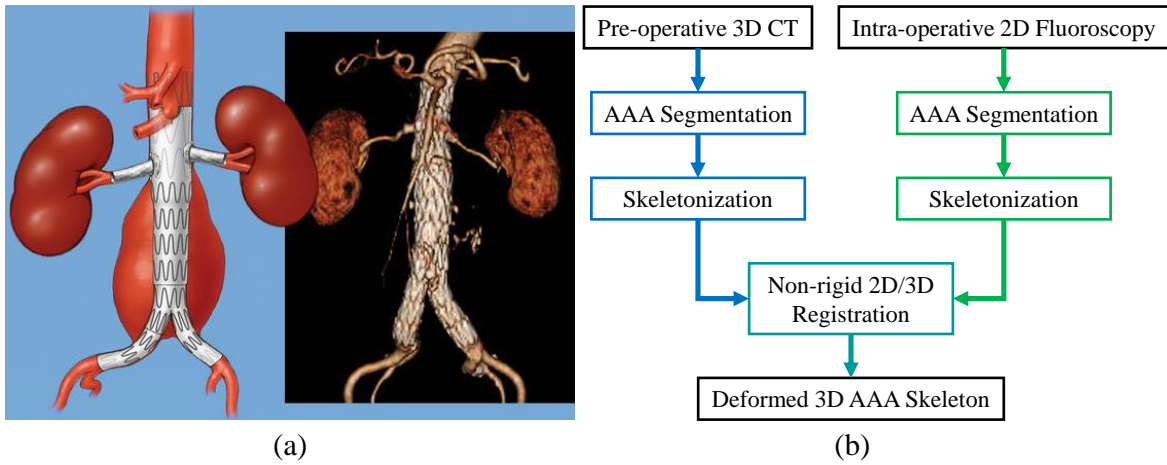


Figure 1.1: (a) A schematic diagram and a 3D reconstructed post-operative shape of FEVAR for a juxtarenal AAA with fenestrated stent-graft [1]; (b) A simple flow chart of 3D robotic path planning for FEVAR

1.1 Background

Abdominal aortic aneurysm (AAA), a considerable health care burden in developed countries, mostly occurs among those who are over 65 years old [2]. It is defined as over 50% excessing of a full-thickness, segmental abdominal aorta dilation [3]. The probability of rupture is related to the aneurysm size [3]. Until aneurysms rupture, usually they are asymptomatic [2]. However, the rupture of aneurysms is significantly lethal with 85 to 90% of mortality [3]. In order to repair the aneurysms, there are three approaches, open repair first performed in 1950, endovascular aneurysm repair (EVAR) performed since 1987 and Fenestrated Endovascular Aneurysm Repair (FEVAR) [4][5][6].

In open repair, one flank or abdominal incision is required. The vessels above and below the abdominal aortic aneurysm are restrained and a synthetic graft is interposed after opening the aneurysm sac [3]. EVAR basically includes the location of a stent graft and the fixation of stent to the normal iliac wall and aortic [2]. As stated by K. Craig Kent [3], the 30-day mortality and the hospital stay in open repair is higher and longer than in EVAR. It is shown that in-hospital and 30-day mortalities of EVAR were only one-third of those of open repair [4]. Therefore, the proportion

of endovascular against open aneurysm repair has increased more than tenfold in the past decade [3]. However, infrarenal EVAR is unsuitable for a part of the patients whose aneurysms cross the branches. The fenestrated endovascular aneurysm repair, first described in 1996 [7], is designed for this kind of cases. As shown in the fig.1.1(a), to access branched arteries, fenestrations are utilized in the graft or scallops and cannulations through the holes are sealed with a covered stent [7]. Each stent graft is customised for an individual patient according to the results of CT angiography [6]. In FEVAR, surgeons first make a minimal incision on one groin of a patient [8]. An introducer sheath is inserted in the incision to pass a catheter and a guidewire inside [8]. Under the guidance of a real-time 2D fluoroscopy, a surgeon controls the catheter to go through the abdominal aorta for stent placement. In this step, the interaction of the catheter or guidewire and the vessel linings is required to be minimized [7]. After the catheter reaching to the right spot, surgeons perform stenting and aneurysmectomy [7].

Currently, there are numerous unanswered questions and limitations in the established FEVAR. First, the real-time 2D image data are usually achieved by X-ray based imaging methods, that leads to an exposure of patients and surgeons to extensive radiation doses [9]. Secondly, this procedure guided by 2D image data from real-time fluoroscopy cannot supply 3D anatomical data to surgeons. Increasing the difficulty and duration of FEVAR, this limitation also raises radiation doses of both patients and surgeons[10]. In addition, due to the lack of anatomical information in three-dimension, the probability of interactions between catheters and vessel linings is increased, which might cause complications including embolization and thrombosis [11]. Therefore, the 3D robotic path planning is required to improve the performance of FEVAR.

1.2 Literature Review

1.2.1 2D Segmentation

The first stage of 3D robotic path planning for FEVAR is segmentation of abdominal aortic aneurysm tissue in each 2D cross-section image. In this project, CT scan is the pre-operative image data source and deep learning is applied to the segmentation of tissues. Therefore, this literature review will mainly focus on the segmentation methods of deep learning. In the early stage, Convolutional Neural Networks (CNNs) was employed to implement segmentation by individually classifying each pixel of one image according to the patches features around the specified pixel [12]. A main drawback of this method is inefficiency, because input patches obtained by this simple sliding window results in huge overlaps of neighboring pixels and repeated computation of the same convolutions [12]. To improve the performance on segmentation, several region-proposal based methods for segmentation was described, utilizing the features extracted by CNNs [13][14]. Recently, fully convolutional networks are increasingly applied to semantic segmentation due to its end-to-end training pattern and efficient feature generation [13][15].

Region based convolutional neural networks (R-CNN), introduced by R. Girshick et al. in 2014 [14], is a typical region proposal based approach. There are four principal steps in the algorithm of R-CNN. First, a sliding window is utilized to check each region in an image to search for specified objects regardless the shape of region [14]. Secondly, a deep CNN is applied to feature extraction in each region of interest (RoI) after affine wrapping [14]. Then the extracted features are input into a linear support vector machine (SVM) within several specific classes [14]. Finally, the boundary of each candidate region is subtly modified by regression methods to segment the specified objects [14]. Taking the advantages of CNNs feature extraction and SVMs classification performance, R-CNN solve the segmentation problem

based on object detection. However, several difficulties hinder the direct application of R-CNN, including the high requirement of disk space caused by the pre-extracted potential region image, the loss of information due to the procedure of cropping or wrapping, and the inefficiency computation results from overlaps between selected regions [12]. Based on R-CNN, several approaches [16][17][18] were proposed. Aiming to improve the performance of R-CNN, R. Girshick proposed fast R-CNN in 2015 [16]. In the study of fast R-CNN, a simple pooling layer for RoI and a mapping function of candidate regions was introduced to improve the training speed of the network by back propagation [16]. In addition, SVMs and bounding box regression are replaced with softmax loss and smoothL1 loss respectively, and the processes of classification and regression are merged to increase accuracy and robustness [16]. This approach has much better performance on accuracy and training efficiency [16]. But the step of a region proposal still takes a long period in training phase [12]. Faster R-CNN, proposed by S. Ren, et al. in 2016 [17], introduced a region proposal network (RPN) as another branch in the networks. Instead of extraction in an original image, the RPN implement region proposal in features matrices, reducing the computation in redundant image data [17]. Furthermore, on the base of faster R-CNN, K. He, et al. proposed mask R-CNN in 2018 [18]. In this network, RoIA-ligh layer replacing RoIPooling layer utilized bilinear interpolation before pooling to avoid errors caused by misalignment [18].

In addition to region proposal based approaches, the fully convolutional network was proposed by J. Long, E. Shelhamer and T. Darrell in 2015 [19] to implement a semantic segmentation network (FCN) trained end-to-end and pixels-to-pixels [19]. Replacing the fully connected layers at the end of a conventional CNN with convolutional layers, those images larger than training ones can be input into the FCN to produce a map of the likelihood instead of only one classification result [12]. Transpose convolution, as a kind of up-sampling operation which also called decon-

volution in [19], is applied to mapping of the classified results to the original image for semantic segmentation. However, due to the operation of pooling layers, output images have far lower resolution than input images [12]. There is a trade-off between spatial resolution and field size of view. To improve the poor resolution, shift-and-stitch was proposed by J. Long et al. [19], in which FCN is applied to a shifted input image and an output image with a full resolution can be obtained by stitching those results together [19]. Taking the idea of the FCN, O. Ronneberger, et al. proposed the architecture of U-net [20] consisting of a regular FCN followed with up-sampling layers to form expansive and contractive paths [12]. While up-sampling is not novel to form expansive and contractive paths [19], it, combined with skip-join points, is directly connected to the opposing, expanding and contracting convolution layer [19]. Similar to U-net, an architecture based on FCN was used by Cicek et al. in 2016 [21] for 3D data. An extensive part of U-Net was proposed by F. Milletari et al. in 2016 [22], including a residual block as well as a Dice loss layer instead of the cross-entropy. It is able to minimize the error measurement of segmentation and increasingly used in medical image segmentation [22]. DeepLab utilized the convolution of up-sampling filters for semantic segmentation [15]. The pooling stride number is decreased to one and holes are inserted into the convolution kernel to expand the field of view for each kernel [15]. Combining a fully connected conditional random field, it also has a better performance on location of object boundaries [15].

There are several studies applying artificial neural network to segmentation of AAA [23][24][25]. For example, a deep belief network was utilized to detect, segment, and classify the AAA [23], however, without quantified segmentation results provided. A deep convolutional neural network (DCNN)-based segmentation and quantification of abdominal aortic thrombus [24] was implemented in totally 38 pre- and post-operative subjects to assess the EVAR treatments [24]. A multi-stage network

including a detection network (holistically-nested edge detection network) and a segmentation network (fully convolutional network) was proposed to segment the thrombi from 13 post-operative CTA volumes [25].

1.2.2 2D/3D Registration

Image registration, as a useful tool that can be applied to a wide range of purposes, is a common study task of image analysis. The task is to determine a spatial mapping or transformation. In the process of image registration, a coordinate transform from one medical image to another one is computed according to corresponding points. There are four principal groups of image registration according to the method of image acquisition, including multi-modal registration, multi-view registration, scene-to-model registration and time series (multitemporal) registration [26]. Each image registration approach requires to consider radiometric deformations, the assumed kind of geometric deformations, noise corruption, required registration accuracy and etc, [26]. Because of various types of images and the diversity of degradations, it is hard to design a non-neural network general approach suitable for all image registration tasks [26].

Since the depth information is lost in anatomic visualization of real-time 2D fluoroscopy, it is difficult especially for junior surgeons to operate the catheter within aortas of patients in FEVAR [27]. Advanced 3D visualization is thus required, which can be implemented by multi-view registration between a pre-operative 3D model and an intra-operative 2D image. Most image registration approaches consist of four main steps [26]. The first step is to detect feature points represented by specific characteristics, such as distinctive points, line endings and gravity centres [26]. The second step is to match the feature points in two images according to different feature descriptors and measurement of their similarity [26]. The third one is to estimate a transform model to describe the mapping functions between the two images

to align the pre-operative images with the intra-operative ones [26]. The final step is to transform the pre-operative images to the intra-operative ones by the estimated mapping functions, and to interpolate values in the non-integer coordinates [26]. There are two main classes of feature detection and matching approaches, including Pixel/voxel-based, model-based and feature-based approaches [28].

Pixel/voxel-based approaches merge the step of feature detection into the step of matching, which process images without salient object detection based on the assumption of the correct registration resulting in the highest similarity [28][29]. These approaches apply windows with predefined size to the estimation of correspondence [30][31]. There are two limitations of the pixel/voxel-based approaches. First, if the image is deformed by complex transformation, the rectangular windows are unsuitable for feature matching [28]. The other one is that a region of smooth intensity change without any obvious details can be matched to another smooth region in the other image [28]. Cross-correlation is a classical pixel/voxel-based approach to match image intensities directly regardless of any structural features [30]. Generalized versions of cross-correlation were proposed to handle more complex geometric deformations [30]. Sequential similarity detection (SSD) algorithm, similar to the cross-correlation approach, add the absolute differences of the image intensity values together and utilizes a threshold criterion as a filter to achieve a lower computational complexity with a certain extent of accuracy loss [31]. Other common pixel/voxel-based similarity approaches include normalized correlation, mean square difference [32], mutual information [26][28][29], normalized mutual information [28][29].

Rigid or deformable shape models are utilized in model-based registration approaches [29]. In the process of rigid models, the curves or surfaces or skeletons of vessels are extracted from the two target images and source as inputs of the registration [33][34][35][36]. The process of deformable models is more complex than that

of rigid models because of several additional regularization terms in cost functions [33]. In the process of deformable modelling, the curves or surfaces or skeletons are extracted from just one image, and then they are applied to fitting the other one with elastic deformation [33]. Another issue for deformable models is the asymmetric transformation [33]. Since the point-search strategy is searching corresponding points in one image referring to the other one, some points in one image perhaps cannot be found in the other one and vice versa, which leads to the different results with varying reference images [33]. The final problem is the redundancy caused by high-dimensional geometric feature spaces of deformation fields, in which the feature point can be aligned to multiple positions [33]. It is a difficulty to distinguish between multiple equivalent fields [33]. In several studies, different methods have been proposed to improve the performance of optimization [37][38][35][36]. The length preservation of vessels is used to constrain the solution space in [35][36].

Feature based registration approaches identify the features of landmarks geometrically or anatomically by analysing the pattern of pixel/voxel intensity variation [29]. The landmarks can be natural or manually mounted, and features can be categorized into two groups, point features and line features. The first one includes line intersections, centroids of areas, local curvature discontinuous, corners and etc. [39][40][41][42]. Line features contains general line segments, the contours of objects, etc. [43][44][10]. For example, there is a kind of methods based on spatial relations, which can be applied to registration including ambiguous features detected and locally distorted neighbourhoods [45].

Types of mapping functions are determined according to the amount of used image data [26]. A global transformation is utilized with parameters valid for each area of one image, and on the contrary, the local transformation processes the image as a combination of patches, in which the parameters rely on the coordinate in the image [26].

In addition to the conventional solution, machine learning is also applied to medical image registration. A novel method based on dissimilarity metric for rigid or deformable registration was proposed [46] including the utilization of Bhattacharyya distances. The approximation of dissimilarity metric for the deformable model is adopted using Markov random field modelling [46]. A fast non-rigid image registration approach, called Quicksilver, was introduced by X. Yang et al. [47], Quicksilver applies a deep encoder-decoder network to generate a prediction model for the large deformation diffeomorphic metric mapping [47]. The results of several experiments show that this approach performs fast and accurately [47]. Different from segmentation and classification, it seems that current studies in application of deep learning to medical image analysis have not proposed an efficient and effective techniques integrating deep learning based registration approaches [12].

There are several studies on deformable 2D/3D registration of AAA[10][36][48][49][50]. However, most of them utilized multiple 2D images[10][36][48][49][50]. For example, two fluoroscopic image was used to recover the deformation of skeletons for EVAR in [36]. A disocclusion-based 2D/3D registration of aorta using two or more 2D images is described in [50]. In addition, landmarks were also utilized in the study of [10] and [49]. A deformable 2D/3D registration of vascular from a single fluoroscopic image was implemented in [35], which applied iterative closest point (ICP) to correspondence between 2D and 3D skeletons, introduced the length preservation to constrain the solving space, and used thin plate spline to model and constrain the deformation of AAA skeletons [35].

In this article, the background of FEVAR will be introduced and the literature of the related technologies will be reviewed first. Secondly, the detail of the applied and proposed methods and the verification experiments in the project will be described. Then the qualitative and quantitative results will be illustrated, Finally, the achievements and limitation of the applied and proposed methods will be discussed.

Chapter 2

Methodology

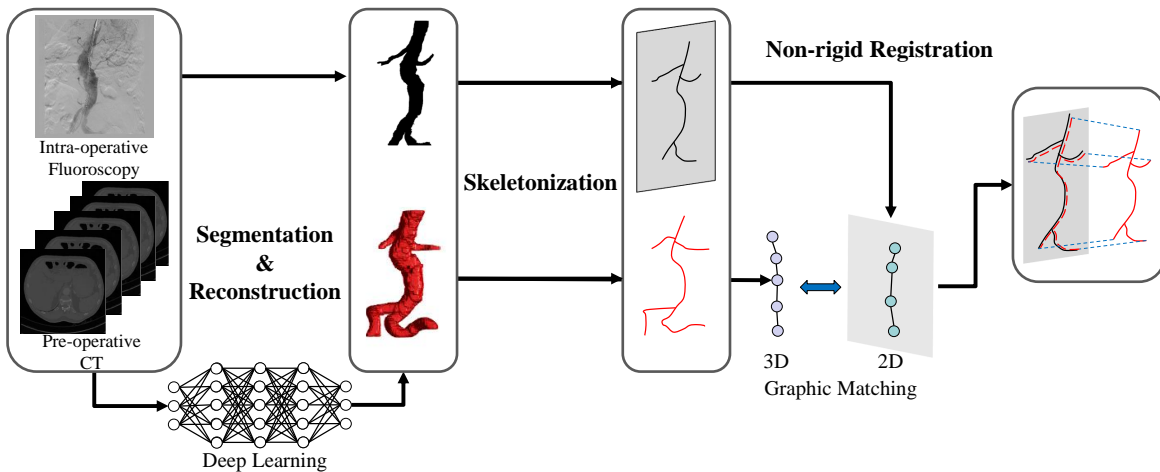


Figure 2.1: Pipeline for Real-time 3D Robotic Path Planning from a Single Fluoroscopic Image for Fenestrated Endovascular Aortic Repair

As shown in the fig.2.1, the total process of the path planning from a single fluoroscopy can be divided into three stages, segmentation&reconstruction, skeletonization and non rigid registration between the 2D and 3D skeletons of AAA, in which a deep convolutional neural network was applied to the stage of segmentation. In the stage of skeletonization, a parallel thinning algorithm for medical axis implemented in [51] was utilized. In the stage of non-rigid registration of 2D and 3D skeletons, a skeleton graph matching approach was proposed and introduced to improve the accuracy and efficiency of registrations.

2.1 Segmentation and Reconstruction

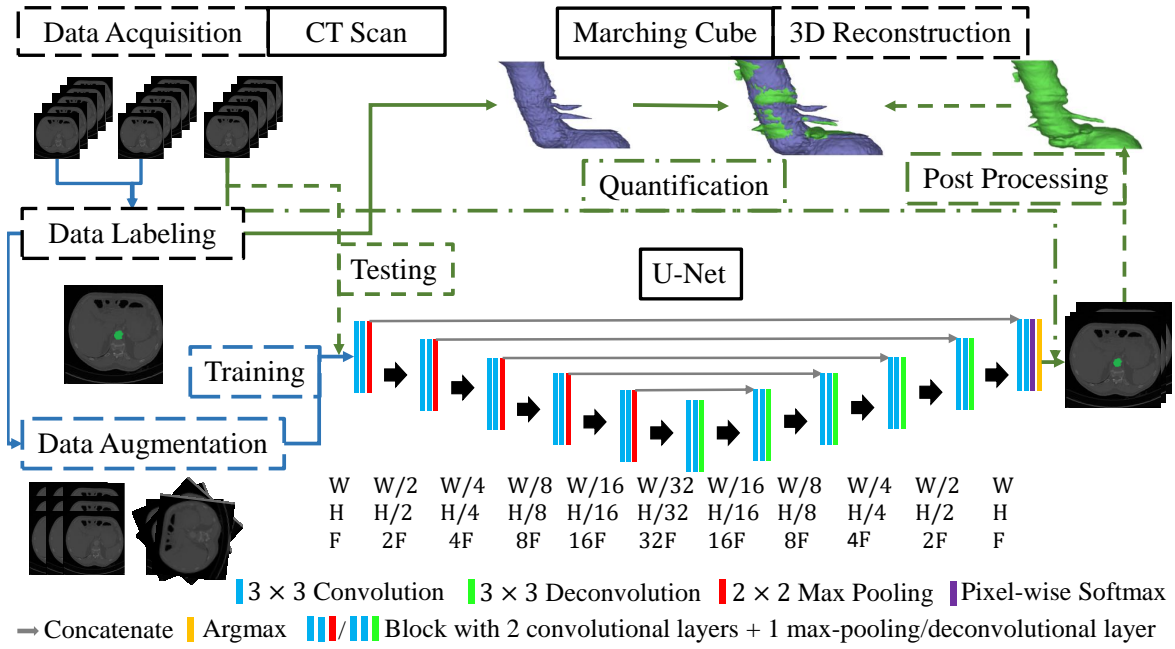


Figure 2.2: Pipeline for 3D AAA segmentation&reconstruction, the 34-layer U-net with a convolution stride as 1, input width $W = 512$, input height $H = 512$, and initial feature number $F = 64$.

The first stage is segmentation and reconstruction of AAA. Fig.2.2 illustrate the sub-pipeline for the first stage, including data acquisition, labeling, augmentation, network training and testing, quantification, post processing and 3D shape reconstruction. The blue lines are for the training subjects and the green ones are for the testing (ground truth) ones.

2.1.1 Data Augmentation

A small number of training subjects results in overfitting due to the inter-subject variations in CT slice contrast (different contrast media used) and the AAA position. In this paper, the inter-subject variation of image contrast was compensated using a linear mapping transformation, and that of AAA position was solved by translating a 512×512 image window along the CT slices with a stride of 64, which called

gray value variation and translation (G.&T.). We also applied rotation and mirroring (R.&M.) data augmentation as a comparison, which was usually used with sufficient training subjects. The data were augmented 45~72 times from hundreds of original slices.

2.1.2 Network Architecture and Training

U-net [20] with convolutional layers, max-pooling layers, and deconvolutional layers was adopted to train and segment the AAA slice-by-slice. Its detailed structure is shown in Fig. 2.2. The input is a 2D CT slice while the output is the segmentation result. Cross-entropy was computed as the loss function:

$$\mathcal{L}_{\text{CE}} = - \sum_{i=1}^W \sum_{j=1}^H \sum_{k=1}^N GT_{(i,j,k)} \log(PP_{(i,j,k)}) \quad (2.1)$$

Here, GT is the ground truth; PP is the predicted probability; W is the image width; H is the image height; $N = 2$ is the class number.

Stochastic Gradient Descent (SGD) and Adam were employed to minimize the loss function with the batch size as 1 and no batch accumulation. For SGD, the initial learning rate was 0.1 and multiplied by 0.1 when the loss stops decreasing. A momentum of 0.9 was applied. The initial learning rate of Adam was 0.001. The loss converged after about 110k iterations (8~12 hours).

2.1.3 Post-processing and 3D Reconstruction

MATLAB[®] functions *regionprops* and *bwareopen* were used to automatically extract the largest volume from the segmentation results. The 3D AAA shape was reconstructed using the marching cube.

2.2 Skeleton Extraction

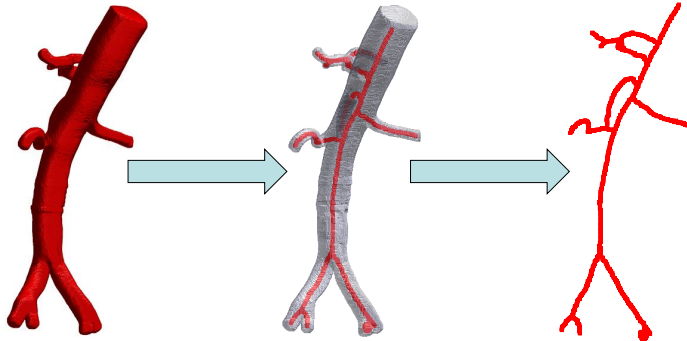


Figure 2.3: Skeletonization of a phantom AAA, with the left picture showing a segmented AAA and the right picture showing the skeleton

The second stage is to extract the skeletons of AAA from 2D fluoroscopic image or 3D CT volume. A parallel algorithm for the medical axis thinning of an arbitrary 3D binary volume described in [52] was implemented in *MATLAB*[®] by Kerschnitzki, Kollmannsberger et al. [51]. The program is used to extract the skeleton of 2D and 3D AAA from intra-operative fluoroscopy and pre-operative CT respectively. The obtained skeleton curve is one pixel wide. One example of skeletonization is demonstrated in the fig.2.3.

2.3 2D/3D Registration of Skeletons

The third stage is 3D to 2D non-registration of the skeletons. Before the non-rigid registration, a rigid initial alignment between 2D and 3D skeletons is required to obtain a calibrated setting denoted as the projection mapping $f : \mathbb{R}^{3 \times n} \rightarrow \mathbb{R}^{2 \times n}$ with a projection matrix $P = \begin{pmatrix} p_1 & p_2 & p_3 \end{pmatrix}^\top \in \mathbb{R}^{3 \times 4}$.

$$f(Y) = \begin{pmatrix} p_1^\top Y^h \odot p_3^\top Y^h \\ p_2^\top Y^h \odot p_3^\top Y^h \end{pmatrix} \quad (2.2)$$

in which \oslash is Hadamard division, $\mathbf{Y} = \begin{pmatrix} \mathbf{y}_1 & \dots & \mathbf{y}_n \end{pmatrix} \in \mathbb{R}^{3 \times n}$ is the matrix consisting of the 3D points' vectors, and $\mathbf{Y}^h = \begin{pmatrix} \mathbf{y}_1^h & \dots & \mathbf{y}_n^h \end{pmatrix} = \begin{pmatrix} \mathbf{Y}^\top & (\mathbf{1})_{n \times 1} \end{pmatrix}^\top \in \mathbb{R}^{4 \times n}$ is the homogeneous vector form of the 3D points.

The problem of rigid registration between 2D and 3D skeletons has been successfully solved for the projection matrix [42][53][54]. In addition, rotational angiography is used in some hospital to sample the intra-operative 3D data, in which the projection matrix can be directly obtained from the calibration parameter and the operation table position [35][55]. Thus, it will not be in the scope of this article.

Graph matching (GM), playing an important role to solve assignment and correspondence problems, is a basic problem in computer science. GM problems that incorporate pair-wise constraints can be formulated as a quadratic assignment problem (QAP) [56][57]. In spite of wide utilization, there are two main limitation for solving the correspondence problem using GM; the first one is that the QAP is difficult to approximate as an NP-hard problem; and the second one is that GM algorithms, focusing on topological properties, excludes the geometric constraints between graph nodes [56][57].

To solve the first problem, a softassignment of 2D and 3D nodes based on the path length of branches is proposed in section 2.3.3. The length preservation term [35] and smoothness constraint term [36] are used as the geometric structural constraint in section 2.3.4 for the second problem. The pipeline for non-rigid 2D/3D registration is shown in the fig.2.4, including four steps, skeleton graph construction, node classification, branch and trunk node matching, and iterative optimization. The overall algorithm of the proposed method for a deformable 2D/3D registration of AAA skeletons is shown in algorithm 1.

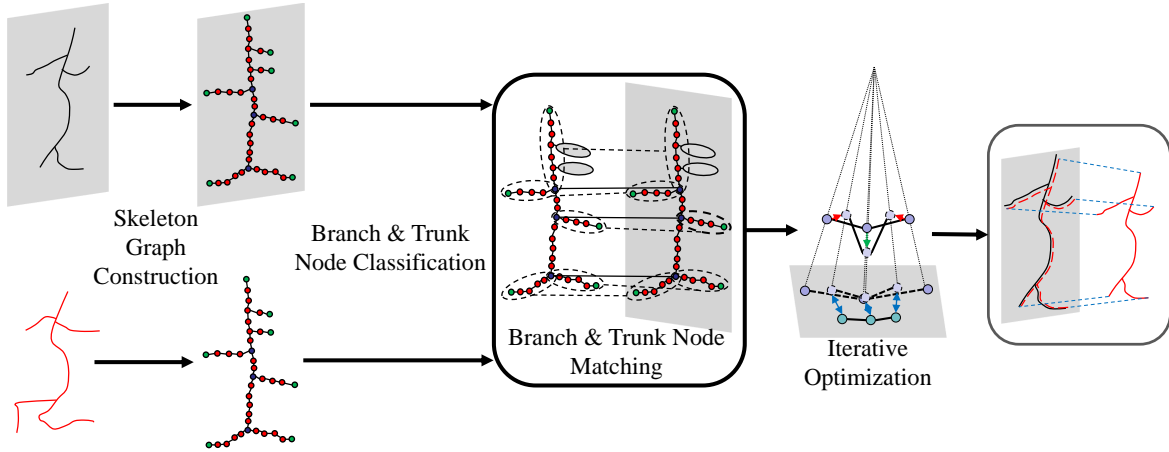


Figure 2.4: Pipeline for non-rigid 2D/3D registration of skeletons

2.3.1 Skeleton Graph Construction

We suppose that the 2D/3D skeleton can be modeled as an undirected simple graph, $\mathbf{G}^d = \langle \mathbf{V}^d, \mathbf{E}^d \rangle$, $d \in \{2, 3\}$ with a set of $|\mathbf{V}^d| = n^d$ nodes $\mathbf{V}^d = \{v_i^d\}_{i \in I^d} \subset \mathbb{R}^d$ corresponding to a 2D/3D skeleton points' matrix $\mathbf{X}^d = (\mathbf{x}_1 \ \dots \ \mathbf{x}_{n^d}) \in \mathbb{R}^{d \times n^d}$, and the edge set $\mathbf{E}^d \subset \mathbf{V}^d \times \mathbf{V}^d$, in which $I^d = [1, n^d] \cap \mathbb{Z}$ is the index set of \mathbf{V}^d . The dimension number d is omitted when an expression is applied to both $d = 2$ and $d = 3$.

Definition 1. Two pixel nodes at the same skeleton are adjacent if their Chebyshev distance is less or equal to 1:

$$a_{i,j} := \begin{cases} 0, & \|\mathbf{x}_i - \mathbf{x}_j\|_\infty > 0 \\ 1, & \|\mathbf{x}_i - \mathbf{x}_j\|_\infty \leq 0 \end{cases} \quad (2.3)$$

where $a_{i,j}$ is the i^{th} row j^{th} column element of \mathbf{G} 's adjacency matrix:

$$\mathbf{A} = \begin{pmatrix} a_{11} & \dots & a_{1n} \\ \vdots & \ddots & \vdots \\ a_{n1} & \dots & a_{nn} \end{pmatrix} \in \mathbb{Z}^{n \times n} \quad (2.4)$$

Definition 2. A pixel point at one skeleton is an end-node if and only if it has one

Algorithm 1: Deformable 2D-3D Registration

Input: X, Y, R, T
Output: Φ, I_d

```

1  $(\mathbf{G}^3 = \langle \mathbf{V}^3, \mathbf{E}^3 \rangle) \leftarrow \text{SKELETON\_GRAPH}(\mathbf{Y});$ 
2  $(\Omega^3, \Pi^3, \mathbf{I}_e^3, \mathbf{I}_c^3, \mathbf{I}_d^3) \leftarrow \text{NODE\_CLASSIFICATION}(\mathbf{G}^3);$ 
3  $(\widehat{\Omega}^3, \widehat{\Pi}^3, \widehat{\mathbf{I}}_c^3) \leftarrow \text{BRANCH\_AND\_TRUNK\_MATCHING}(\mathbf{Y}, \Omega^3, \Pi^3, \mathbf{I}_c^3);$ 
4  $(\mathbf{G}^2 = \langle \mathbf{V}^2, \mathbf{E}^2 \rangle) \leftarrow \text{SKELETON\_GRAPH}(\mathbf{X});$ 
5  $(\Omega^2, \Pi^2, \mathbf{I}_e^2, \mathbf{I}_c^2, \mathbf{I}_d^2) \leftarrow \text{NODE\_CLASSIFICATION}(\mathbf{G}^2);$ 
6  $(\widehat{\Omega}^2, \widehat{\Pi}^2, \widehat{\mathbf{I}}_c^2) \leftarrow \text{BRANCH\_AND\_TRUNK\_MATCHING}(\mathbf{X}, \Omega^2, \Pi^2, \mathbf{I}_c^2);$ 
7 initialize the assignment matrix  $\mathbf{M} = \begin{pmatrix} m_{11} & \dots & m_{1n^3} \\ \vdots & \ddots & \vdots \\ m_{n^2 1} & \dots & m_{n^2 n^3} \end{pmatrix} \leftarrow (0)_{n^2 \times n^3};$ 
8  $\mathbf{M} \leftarrow \text{BRANCH\_NODE\_ASSIGNING}(\widehat{\Omega}^2, \widehat{\Omega}^3, \mathbf{X}, \mathbf{Y}, \mathbf{M});$ 
9  $\mathbf{M} \leftarrow \text{TRUNK\_NODE\_ASSIGNING}(\widehat{\Pi}^2, \widehat{\Pi}^3, \mathbf{X}, \mathbf{Y}, \mathbf{M});$ 
10 if  $\sum_{i=1}^{n^2} m_{i,j} = 0$  then
11   label  $y_j$  as unassigned,  $\forall j \in \mathbf{I}^3 \setminus \mathbf{I}_d^3;$ 
12 initialized displacement vectors for assigned nodes,  $\Phi'$ ;
13 while not convergence do
14   compute  $\nabla \varepsilon(\Phi') = \nabla S_D(\Phi') + \alpha \nabla S_L(\Phi') + \beta \nabla S_S(\Phi');$ 
15   update  $\Phi'$ 
16 compute the displacement vectors  $\Phi$  using branch-wise 3D TPS for the
   unassigned nodes;
17 return  $\Phi, I_d.$ 

```

adjacent point:

$$\mathbf{I}_e := \{i | \deg(v_i) = 1, v_i \in \mathbf{V}(\mathbf{G})\} \quad (2.5)$$

in which $\deg(\cdot)$ is the degree of a node, $\mathbf{I}_e \subseteq \mathbf{I}$ is the index number set of the end-nodes in \mathbf{V} .

Denote the set and the index number set of the pixel points which has three or more adjacent points as the set and the index number set of quasi-junction-nodes in \mathbf{V} :

$$\mathbf{I}_{q-c} := \{i | \deg(v_i) \geq 3, v_i \in \mathbf{V}(\mathbf{G})\} \quad (2.6)$$

Construct the subgraph $\mathbf{G}_{q-c} \subseteq \mathbf{G}$, including all the junction-nodes and their in-

Algorithm 2: Skeleton Graph

Input: $\mathbf{X} = (x_1 \ \dots \ x_n)$
Output: \mathbf{G}

```

1  $(d, n) \leftarrow \text{size}(\mathbf{X})$ 
2  $\mathbf{V} = \{v_i\}_{i \in I}, \quad I = [1, n] \cap \mathbb{Z};$ 
3 initialize an adjacency matrix  $\mathbf{A} = \begin{pmatrix} a_{11} & \dots & a_{1n} \\ \vdots & \ddots & \vdots \\ a_{n1} & \dots & a_{nn} \end{pmatrix} \leftarrow (0)_{n \times n};$ 
4 for  $i = 1$  to  $n$  do
5   for  $j = 1$  to  $n$  do
6     if  $\|\mathbf{x}_i - \mathbf{x}_j\|_\infty \leq 0$  then
7        $a_{i,j} \leftarrow 1;$ 
8        $E \leftarrow E \cup \{(v_i, v_j)\};$ 
9     else
10     $a_{i,j} \leftarrow 0;$ 
11    $w_{i,j} \leftarrow \infty;$ 
11 return  $\mathbf{G} = \langle \mathbf{V}, E \rangle$ 

```

terconnection edges: $\mathbf{V}(\mathbf{G}_{q-c}) = \{v_i\}_{i \in I_{q-c}}$ and $\mathbf{E}(\mathbf{G}_{q-c}) = \{(v_i, v_j) | i, j \in I_{q-c}, i \neq j\} \cap \mathbf{E}(\mathbf{G})$.

Definition 3. *The node having the largest degree among each connected component of \mathbf{G}_{q-c} is defined as a junction-node, and the index number set of junction-nodes is denoted as I_c . Those nodes which are neither end-nodes nor junction-nodes are defined as connection-nodes.*

Definition 4. *A sequence of nodes on the shortest path between and including an end-node and the neighbouring junction-node is defined as a branch with the vector of their indexes denoted as $\omega \in \Omega$, in which Ω is the set of the index number vectors of all the branches. A sequence of nodes on the shortest path between and including two neighbouring junction-nodes is defined as a trunk with the vector of their index numbers denoted as $\pi \in \Pi$, Π is the set of the index number vectors of all the trunks.*

In addition, a rough surface or a large error of segmented shape might results in unexpected branches other than the expected ones in ideal case. In the procedure

of registration, the skeleton node sequence of left/right renal arteries, left/right common iliac arteries and the upper aorta are specified as the five expected preserved branches for registration, which are assumed as the longest five segmented branches. The unexpected branches are called pseudo branches; the end-nodes and connection-nodes of pseudo branches are pseudo nodes; the junction-nodes of pseudo branches are pseudo junction-nodes.

2.3.2 Node Classification

Algorithm 3: Skeleton Node Classification

Input: $G = \langle V, E \rangle$

Output: $\Omega, \Pi, I_e, I_c, I_d$

```

1 for  $i = 1$  to  $n$  do
2   if  $\deg(v_i) = 1$  then
3      $I_e \leftarrow I_e \cup \{i\};$ 
4   else
5     if  $\deg(v_i) \geq 3$  then  $I_{q-c} \leftarrow I_{q-c} \cup \{i\};$ 
5 construct
6    $G_{q-c} \subseteq G : V(G_{q-c}) \leftarrow \{v_i\}_{i \in I_{q-c}}, E(G_{q-c}) \leftarrow \{(v_i, v_j) | i, j \in I_{q-c}, i \neq j\} \cap E(G);$ 
6 foreach connected component of  $G_{q-c}$  denoted as  $C(G_{q-c})$  do
7    $I_c \leftarrow I_c \cup \arg \max_i \{\deg(v_i) : v_i \in V(C(G_{q-c}))\};$ 
8    $(\Omega, I_c, I_d) \leftarrow \text{BRANCH\_NODE\_SEARCHING}(G, I_e, I_c);$ 
9    $\Pi \leftarrow \text{TRUNK\_NODE\_SEARCHING}(G, I_c, I_d);$ 
10 return  $\Omega, \Pi, I_e, I_c, I_d$ 

```

Before the step of node classification, it is required to specify the skeleton branches of five arteries as the preserved branches, which are assumed as the longest five branches. A Breadth First Search (BFS) algorithm with a shortest path algorithm embedded is proposed to group each sequence of connection-node into branch or trunk with the corresponding end-node and junction-node, or with the two corresponding junction-nodes, as well as to obtain the shortest path distance of each connection-node from the corresponding junction-node(s), and thus to detect the

Algorithm 4: Branch Node Searching based on Dijkstra's Algorithm

Input: $G = \langle V, E \rangle, I_e, I_c$ **Output:** Ω, I_c, I_d

```

1 foreach  $i \in I_e$  do
2   initialize a list  $p_i(v) \leftarrow \emptyset, \forall v \in V(G)$ ;
3   initialize a list  $s_i(v) \leftarrow \infty, \forall v \in V(G)$ ;
4    $s_i(v_i) \leftarrow 0$ ;
5   initialize a set  $\sigma_i \leftarrow \emptyset$ ;
6 while  $I_e \neq \emptyset$  do
7   foreach  $i \in I_e$  do
8     copy  $s'_i \leftarrow \min_j \{s_i(v_j) : v_j \in V(G), j \notin (\sigma_i \cup I_d)\}$ ;
9     while  $s'_i = \min_j \{s_i(v_j) : v_j \in V(G), j \notin (\sigma_i \cup I_d)\}$  do
10     $j \leftarrow \arg \min_j \{s_i(v_j) : v_j \in V(G), j \notin (\sigma_i \cup I_d)\}$ ;
11    if  $j \in I_c$  then
12       $I_e \leftarrow I_e \setminus \{i\}$ ;
13       $k \leftarrow j$ ;
14      while  $k \neq \emptyset$  do
15         $\omega \leftarrow (\omega, k)$ ;
16         $k \leftarrow p_i(v_k)$ ;
17      if  $|I_e| > \tau$  then
18         $I_c \leftarrow I_c \setminus \{j\}$ ;
19        if  $|\omega| < \iota$  then
20           $I_d \leftarrow I_d \cup \omega$ ;
21      else
22         $\Omega \leftarrow \Omega \cup \{\omega\}$ 
23       $\sigma_i \leftarrow (\sigma_i, j)$ ;
24      foreach  $u \in \Gamma(v_j)$  do
25        if  $s_i(u) > s_i(v_j) + 1$  then
26           $s_i(u) \leftarrow s_i(v_j) + 1$ ;
           $p_i(u) \leftarrow j$ ;
27 return  $\Omega, I_c, I_d$ 

```

pseudo nodes and branches.

In the algorithm of node classification (as shown in the algorithm 3), the graph of a 2D or a 3D skeleton \mathbf{G} is input and the output includes the index number sets of the end-nodes I_e , the junction-nodes I_c and the pseudo nodes I_d , as well as the set of all branches' index number vectors Ω and the set of all trunks' index number vectors Π . In brief, first, all the end-nodes and quasi-junction-nodes are searched; secondly, the subgraph including all the quasi-junction-nodes is constructed and the junction-nodes are extracted; thirdly, the nodes of each branch are searched and the branches are classified as to be preserved or omitted or deleted using the algorithm 4; finally, the nodes of each trunk are searched using the algorithm 5.

In the algorithm of branch node searching, the graph of 2D or 3D skeleton \mathbf{G} , the index number sets of the end-nodes I_e and the junction-nodes I_c are input, and the set of all branches' index number vectors Ω , a new index number set of the junction-nodes I_c and the pseudo nodes I_d are output. In this algorithm, each end-nodes are initialized as unmarked first. The shortest path from each unmarked end-node to the neighbouring junction-node is then searched by exploring the adjacent nodes at the present depth prior to moving on to the next depth level. Each time when the shortest path is found between one unmarked end-node and the neighbouring junction-node, the end-node is marked, and the length of this path and the number of unmarked end-nodes are compared respectively with the threshold geodesic length of pseudo branches denoted as ι and the threshold number of preserved branches denoted as τ . Those branches whose geodesic length is shorter than ι are classified as pseudo nodes and deleted in the latter steps and their junction-nodes are converted to connection-nodes, the longest $\tau(:=5)$ branches are preserved with the vector of their indices stored in Ω , and the junction-nodes for the other branches are also converted to connection-nodes.

In the algorithm of trunk node searching, the graph of the 2D or 3D skeleton \mathbf{G} ,

Algorithm 5: Trunk Node Searching based on Dijkstra's Algorithm

Input: $G = \langle V, E \rangle, I_c, I_d$
Output: Π

```

1 foreach  $i \in I_c$  do
2   initialize a list  $p_i(v) \leftarrow \emptyset, \forall v \in V(G)$ ;
3   initialize a list  $s_i(v) \leftarrow \infty, \forall v \in V(G)$ ;
4    $s_i(v_i) \leftarrow 0$ ;
5   initialize a set  $\sigma_i \leftarrow \emptyset$ ;
6 copy  $I'_c \leftarrow I_c$ ;
7 while  $I'_c \neq \emptyset$  do
8   foreach  $i \in I_c$  do
9      $j \leftarrow \arg \min_j \{s_i(v_j) : v_j \in V(G), j \notin (\sigma_i \cup I_d)\}$ ;
10    foreach  $l \in I'_c \setminus \{i\}$  do
11      if  $j \in \sigma_l$  then
12         $I'_c \leftarrow I'_c \setminus \{i, l\}$ ;
13         $k \leftarrow j$ ;
14        while  $k \neq \emptyset$  do
15           $\pi \leftarrow (k, \pi)$ ;
16           $k \leftarrow p_i(v_k)$ ;
17         $k \leftarrow j$ ;
18        while  $k \neq \emptyset$  do
19           $k \leftarrow p_i(v_k)$ ;
20           $\pi \leftarrow (\pi, k)$ ;
21         $\Pi \leftarrow \Pi \cup \{\pi\}$ 
22       $\sigma_i \leftarrow (\sigma_i, j)$ ;
23      foreach  $u \in \Gamma(v_j)$  do
24        if  $s_i(u) > s_i(v_j) + 1$  then
25           $s_i(u) \leftarrow s_i(v_j) + 1$ ;
26           $p_i(u) \leftarrow j$ ;
27 return  $\Pi$ 

```

the index number sets of the junction-nodes I_c and the pseudo nodes I_d are input, and the set of all trunks' index number vectors Π is output. In this algorithm, each junction-node are initialized as unmarked first. The shortest path between each two neighbouring junction-node is searched using bidirectional BFS, in which at least one junction-node is unmarked. The found paths are preserved as trunks with the vector of their indices stored in Π .

It is noteworthy that the path length of branches in the node classification is calculated as the geodesic distance for the efficiency of the algorithm, which is different from the path length in the algorithm 7 and algorithm 8. The shortest path searching in these algorithms can be implemented based on Dijkstra's algorithm [58], the adjacency matrix product. The pseudo code for the branch node searching based on the Dijkstra's algorithm is given as the algorithm 4, and the pseudo code for the trunk node searching based on the Dijkstra's algorithm is shown in the algorithm 5.

2.3.3 Node Matching

Branch and Trunk Matching

An algorithm as shown in the algorithm 6 is proposed to match branch and trunk for both 2D and 3D skeleton graphs referring to the structure of AAA, in which the nodes' coordinates, the graph, the index number sets of branches and trunks and junction-nodes are input, and the ordered index number sets of branches and trunks and junction-nodes are output. In the algorithm, the junction-nodes and trunks are ordered first according to the path length of these trunks; secondly, the tangent vectors of branches at the corresponding junction-nodes T are approached secondly using the vector from the starting point with an index η_s to the terminating point with an index η_t , and the similarity matrix S of the tangent vectors is calculated to evaluate the direction difference between the tangents of the branches; finally, the

branches are ordered according to the similarity matrix and matched in 2D and 3D.

The assignment matrix $\mathbf{M} = \begin{pmatrix} m_{11} & \dots & m_{1n^3} \\ \vdots & \ddots & \vdots \\ m_{n^21} & \dots & m_{n^2n^3} \end{pmatrix} \in \mathbb{R}_+^{n^2 \times n^3}$ is initialized as:

Algorithm 6: Branch and Trunk Matching

Input: $X, G = \langle V, E \rangle, \Omega, \Pi, I_c$

Output: $\widehat{\Omega}, \widehat{\Pi}, \widehat{I}_c$

-
- 1 obtain ordered list \widehat{I}_c from I_c referring to Π ;
 - 2 obtain ordered list $\widehat{\Pi}$ from Π referring to \widehat{I}_c ;
 - 3 initialize the tangent vector matrix $\mathbf{T} = (\mathbf{t}_1 \ \dots \ \mathbf{t}_{|\Omega|}) \in \mathbb{R}^{d \times |\Omega|}$;
 - 4 **foreach** $\omega_i \in \Omega$ **do**
 - 5 $\mathbf{t}_i \leftarrow X[\omega_i[\eta_t]] - X[\omega_i[\eta_s]]$;
 - 6 calculate tangent similarity matrix $S \leftarrow \mathbf{T}^\top \mathbf{T}$;
 - 7 obtain ordered list $\widehat{\Omega}$ from Ω referring to \widehat{I}_c and S ;
 - 8 **return** $\widehat{\Omega}, \widehat{\Pi}, \widehat{I}_c$
-

$$m_{(i,j)} = 0, \forall i \in [1, n^2] \cap \mathbb{Z}, j \in [1, n^3] \cap \mathbb{Z} \quad (2.7)$$

Branch Node Assigning

The algorithm 7 describes the softassigning between the 2D nodes and the projected 3D nodes at each matched pair of branches, referring to the path length from the corresponding junction-node.

A set of 2D nodes are generated with the same number as the projection of the matched 3D skeleton branch using linear interpolation of the two adjacent nodes at the same 2D branch:

$$\begin{cases} \mathbf{x}'_j = m_{(\omega_i^2, \omega_j^3)} \cdot \mathbf{x}_{\omega_i^2} + m_{(\omega_{i+1}^2, \omega_j^3)} \cdot \mathbf{x}_{\omega_{i+1}^2} \\ m_{(\omega_i^2, \omega_j^3)} + m_{(\omega_{i+1}^2, \omega_j^3)} = 1 \\ 0 \leq m_{(\omega_i^2, \omega_j^3)} \leq 1 \end{cases} \quad (2.8)$$

Algorithm 7: Branch Node Assigning

Input: $\widehat{\Omega}^2, \widehat{\Omega}^3, X, Y, M$ **Output:** M

```

1 for  $i = 1$  to  $|\widehat{\Omega}^2|$  do
2    $j \leftarrow 1;$ 
3    $k \leftarrow 1;$ 
4    $c_c^2 \leftarrow 0;$ 
5    $c_f^2 \leftarrow 0;$ 
6    $c_c^3 \leftarrow 0;$ 
7    $c_f^3 \leftarrow 0;$ 
8    $\omega^2 \leftarrow \widehat{\Omega}^2_i;$ 
9    $\omega^3 \leftarrow \widehat{\Omega}^3_i;$ 
10  while  $j \leq |\omega^2|$  and  $k \leq |\omega^3|$  do
11    if  $c_c^2 \leq c_c^3$  then
12       $j \leftarrow j + 1;$ 
13       $c_f^2 \leftarrow c_c^2;$ 
14       $b \leftarrow \|x_{\omega_j^2} - x_{\omega_{j-1}^2}\|_2;$ 
15       $c_c^2 \leftarrow c_f^2 + b;$ 
16    else
17      if  $c_f^2 > c_c^3$  then
18         $k \leftarrow k + 1;$ 
19         $c_f^3 \leftarrow c_c^3;$ 
20         $c_c^3 \leftarrow c_f^3 + \|f(y_{\omega_k^3}) - f(y_{\omega_{k-1}^3})\|_2;$ 
21      else
22         $m_{(\omega_{j-1}^2, \omega_k^3)} \leftarrow \frac{c_c^2 - c_c^3}{b};$ 
23         $m_{(\omega_j^2, \omega_k^3)} \leftarrow \frac{c_c^3 - c_f^2}{b};$ 
24    label  $y_{\omega_i^3}$  as unassigned,  $\forall l \in (k, |\omega^3|] \cap \mathbb{Z};$ 
25 return  $M$ 

```

in which, $\omega \in \Omega$ is one index vector of branch without loss of generality, ω_i is the i^{th} element of ω . It is required to satisfy that the path length from the corresponding junction-node to each interpolated 2D node is the same as that of the assigned projected 3D node:

$$\sum_{k=2}^j \|f(\mathbf{y}_{\omega_k^3}) - f(\mathbf{y}_{\omega_{k-1}^3})\|_2 = \|\mathbf{x}'_j - \mathbf{x}_{\omega_i^2}\|_2 + \sum_{l=2}^i \|\mathbf{x}_{\omega_l^2} - \mathbf{x}_{\omega_{l-1}^2}\|_2 \quad (2.9)$$

in which, $i \in [1, |\omega^2|] \cap \mathbb{Z}, j \in [1, |\omega^3|] \cap \mathbb{Z}$, and define that $\sum_{i=2}^1 (\cdot) := 0$. Then substitute equation 2.8 into equation 2.9 and obtain:

$$\begin{cases} m_{(\omega_{i+1}^2, \omega_j^3)} = \frac{\sum_{k=2}^j \|f(\mathbf{y}_{\omega_k^3}) - f(\mathbf{y}_{\omega_{k-1}^3})\|_2 - \sum_{l=2}^i \|\mathbf{x}_{\omega_l^2} - \mathbf{x}_{\omega_{l-1}^2}\|_2}{\|\mathbf{x}_{\omega_{i+1}^2} - \mathbf{x}_{\omega_i^2}\|_2} \\ m_{(\omega_i^2, \omega_j^3)} = 1 - m_{(\omega_{i+1}^2, \omega_j^3)} \\ 0 \leq m_{(\omega_i^2, \omega_j^3)} \leq 1 \end{cases} \quad (2.10)$$

The equation 2.10 is used to calculate an assignment matrix for the fuzzy and partial correspondence between the branch nodes in 2D and 3D in the algorithm 7.

Trunk Node Assigning

The algorithm 8 describes the softassigning between the 2D nodes and the 3D nodes at each matched pair of branches, referring to the proportion of the path length from the corresponding junction-node.

A set of 2D nodes are generated with the same number as the target 3D skeleton branch using linear interpolation of the two adjacent nodes at the same 2D branch:

$$\begin{cases} \mathbf{x}'_j = m_{(\pi_i^2, \pi_j^3)} \cdot \mathbf{x}_{\pi_i^2} + m_{(\pi_{i+1}^2, \pi_j^3)} \cdot \mathbf{x}_{\pi_{i+1}^2} \\ m_{(\pi_i^2, \pi_j^3)} + m_{(\pi_{i+1}^2, \pi_j^3)} = 1 \\ 0 \leq m_{(\pi_i^2, \pi_j^3)} \leq 1 \end{cases} \quad (2.11)$$

Algorithm 8: Trunk Node Assigning

Input: $\widehat{\Pi}^2, \widehat{\Pi}^3, X, Y, M$
Output: M

```

1 for  $i = 1$  to  $|\widehat{\Pi}^2|$  do
2    $\pi^2 \leftarrow \widehat{\Pi}^2_i;$ 
3    $\pi^3 \leftarrow \widehat{\Pi}^3_i;$ 
4    $\lambda^2 \leftarrow \sum_{j=2}^{|\pi^2|} \|\mathbf{x}_{\pi_j^2} - \mathbf{x}_{\pi_{j-1}^2}\|_2;$ 
5    $\lambda^3 \leftarrow \sum_{j=2}^{|\pi^3|} \|\mathbf{y}_{\pi_j^3} - \mathbf{y}_{\pi_{j-1}^3}\|_2;$ 
6    $j \leftarrow 1;$ 
7    $k \leftarrow 1;$ 
8    $c_c^2 \leftarrow 0;$ 
9    $c_f^2 \leftarrow 0;$ 
10   $c_c^3 \leftarrow 0;$ 
11   $c_f^3 \leftarrow 0;$ 
12  while  $k \leq |\pi^3|$  do
13    if  $c_c^2 \leq c_c^3$  then
14       $j \leftarrow j + 1;$ 
15       $c_f^2 \leftarrow c_c^2;$ 
16      if  $c_f^2 < 1$  then
17         $b \leftarrow \frac{\|\mathbf{x}_{\pi_j^2} - \mathbf{x}_{\pi_{j-1}^2}\|}{\lambda^2};$ 
18      else
19         $b \leftarrow 1;$ 
20         $c_c^2 \leftarrow c_f^2 + b;$ 
21    else
22      if  $c_f^2 > c_c^3$  then
23         $k \leftarrow k + 1;$ 
24         $c_f^3 \leftarrow c_c^3;$ 
25         $c_c^3 \leftarrow c_f^3 + \frac{\|\mathbf{y}_{\pi_k^3} - \mathbf{y}_{\pi_{k-1}^3}\|}{\lambda^3};$ 
26      else
27         $m_{(\pi_{j-1}^2, \pi_k^3)} \leftarrow \frac{c_c^2 - c_c^3}{b};$ 
28         $m_{(\pi_j^2, \pi_k^3)} \leftarrow \frac{c_c^3 - c_f^2}{b};$ 
29
30 return  $M$ 

```

it is required to satisfy that the proportion of the path length from the corresponding junction-node to each interpolated 2D node is the same as that of the assigned 3D node:

$$\frac{\sum_{k=2}^j \|\mathbf{y}_{\pi_k^3} - \mathbf{y}_{\pi_{k-1}^3}\|_2}{\sum_{k=2}^{|\pi^3|} \|\mathbf{y}_{\pi_k^3} - \mathbf{y}_{\pi_{k-1}^3}\|_2} = \frac{\|\mathbf{x}'_j - \mathbf{x}_{\pi_i^2}\|_2 + \sum_{l=2}^i \|\mathbf{x}_{\pi_l^2} - \mathbf{x}_{\pi_{l-1}^2}\|_2}{\sum_{l=2}^{|\pi^2|} \|\mathbf{x}_{\pi_l^2} - \mathbf{x}_{\pi_{l-1}^2}\|_2} \quad (2.12)$$

in which, $i \in [1, |\pi^2|] \cap \mathbb{Z}$, $j \in [1, |\pi^3|] \cap \mathbb{Z}$. Then substitute the equation 2.11 into the equation 2.12 and obtain:

$$\begin{cases} m_{(\pi_{i+1}^2, \pi_j^3)} = \frac{\lambda^2 \sum_{k=2}^j \|\mathbf{y}_{\pi_k^3} - \mathbf{y}_{\pi_{k-1}^3}\|_2 - \sum_{l=2}^i \|\mathbf{x}_{\pi_l^2} - \mathbf{x}_{\pi_{l-1}^2}\|_2}{\|\mathbf{x}_{\pi_{i+1}^2} - \mathbf{x}_{\pi_i^2}\|_2} \\ m_{(\pi_i^2, \pi_j^3)} + m_{(\pi_{i+1}^2, \pi_j^3)} = 1 \\ 0 \leq m_{(\pi_i^2, \pi_j^3)} \leq 1 \end{cases} \quad (2.13)$$

in which, $\lambda^2 = \sum_{l=2}^{|\pi^2|} \|\mathbf{x}_{\pi_l^2} - \mathbf{x}_{\pi_{l-1}^2}\|_2$ and $\lambda^3 = \sum_{k=2}^{|\pi^3|} \|\mathbf{y}_{\pi_k^3} - \mathbf{y}_{\pi_{k-1}^3}\|_2$. The equation 2.13 is used to calculate a assignment matrix for the fuzzy and partial correspondence between the trunk nodes in 2D and 3D in the algorithm 8.

2.3.4 Iterative Optimization for Deformation

The target of deformation is to obtain displacement vectors of the 3D skeleton nodes $\Phi = (\varphi_1 \quad \dots \quad \varphi_{n^3})$ to minimize the energy function ε [35].

$$\Phi' = \arg \min_{\Phi} (\varepsilon) \quad (2.14)$$

in which Φ' is the estimate of Φ , the energy function [35] is written as:

Energy Function

The energy function [35] is written as:

$$\varepsilon(\Phi) = S_D(\Phi) + \alpha S_L(\Phi) + \beta S_S(\Phi) \quad (2.15)$$

in which, S_D is the difference measure term, S_L is the length preservation term with the coefficient α , S_S is the smoothness constraint term with the coefficient β .

Fig.2.5 illustrates the effect of the difference measure and the term of length preservation. The 3D nodes moving along the red arrows are induced by minimizing the distance difference between the projected 3D nodes and the assigned 2D nodes, and the 3D node moving along the green arrow is to minimize the length preservation term. The smoothness constraint term is to avoid the unnatural deformation of the 3D skeleton.

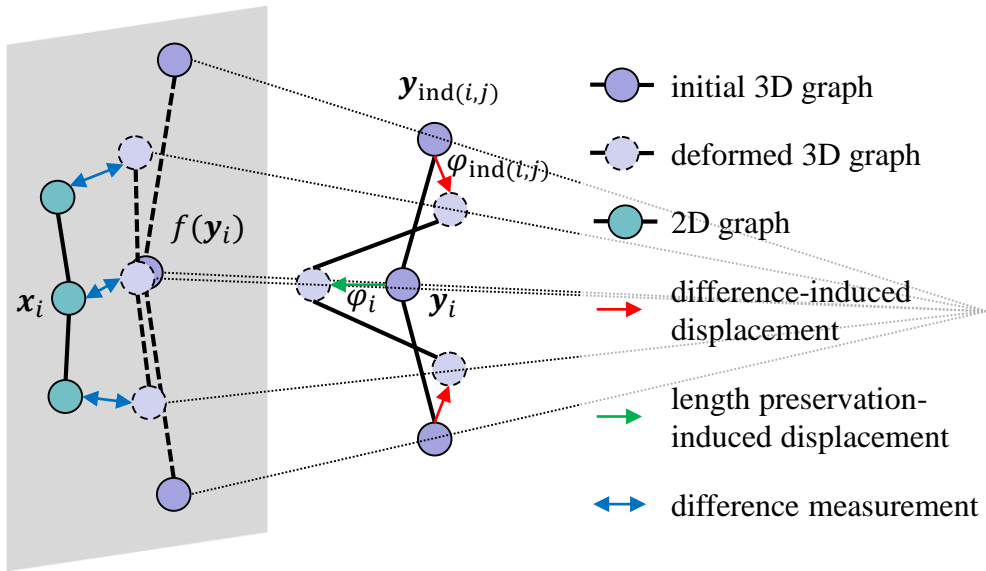


Figure 2.5: Effect of the difference measure and the length preservation constraint

Difference Measure

The term of the difference measure [35] is shown as:

$$S_D = \frac{1}{n^3} \sum_{i=1}^{n^3} \|\mathbf{x}'_i - f(\mathbf{y}_i + \varphi_i)\|_2^2 \quad (2.16)$$

The derivation of S_D with respect to φ_i [35] is given by:

$$\frac{\partial S_D}{\partial \varphi_i} = -\frac{2}{n^3} (\mathbf{x}'_i - f(\tilde{\mathbf{y}}_i))^\top \mathbf{J}_i \quad (2.17)$$

in which $\tilde{\mathbf{y}}_i = \mathbf{y}_i + \varphi$, and $\mathbf{J}_i \in \mathbb{R}^{2 \times 3}$ is the jacobian matrix of projection function f with respect to φ_i [35]:

$$\mathbf{J}_i = \frac{1}{(\mathbf{p}_3^\top \tilde{\mathbf{y}}_i^h)^2} \begin{pmatrix} p_{11}\mathbf{p}_3^\top \tilde{\mathbf{y}}_i^h - p_{31}\mathbf{p}_1^\top \tilde{\mathbf{y}}_i^h & p_{12}\mathbf{p}_3^\top \tilde{\mathbf{y}}_i^h - p_{32}\mathbf{p}_1^\top \tilde{\mathbf{y}}_i^h & p_{13}\mathbf{p}_3^\top \tilde{\mathbf{y}}_i^h - p_{33}\mathbf{p}_1^\top \tilde{\mathbf{y}}_i^h \\ p_{21}\mathbf{p}_3^\top \tilde{\mathbf{y}}_i^h - p_{31}\mathbf{p}_2^\top \tilde{\mathbf{y}}_i^h & p_{22}\mathbf{p}_3^\top \tilde{\mathbf{y}}_i^h - p_{32}\mathbf{p}_2^\top \tilde{\mathbf{y}}_i^h & p_{23}\mathbf{p}_3^\top \tilde{\mathbf{y}}_i^h - p_{33}\mathbf{p}_2^\top \tilde{\mathbf{y}}_i^h \end{pmatrix} \quad (2.18)$$

which implies the jacobian matrix \mathbf{J}_i is calculated respectively for each node in the 3D skeleton. To improve the speed of the program, we edit the equation 2.18 to decompose $\tilde{\mathbf{y}}_i$ from \mathbf{J}_i :

$$\text{vec}(\mathbf{J}_i) = \frac{1}{(\mathbf{p}_3^\top \tilde{\mathbf{y}}_i^h)^2} \mathbf{J}' \tilde{\mathbf{y}}_i^h \quad (2.19)$$

in which, $\text{vec}(\cdot) : \mathbb{R}^{n_1 \times n_2} \rightarrow \mathbb{R}^{n_1 n_2 \times 1}, n_1, n_2 \in \mathbb{Z}_+$ is a vectorization mapping:

$$\text{vec}(\mathbf{J}_i) : \begin{pmatrix} J_{11} & J_{12} & J_{13} \\ J_{21} & J_{22} & J_{23} \end{pmatrix} \mapsto \begin{pmatrix} J_{11} & J_{21} & J_{12} & J_{22} & J_{13} & J_{23} \end{pmatrix}^\top \quad (2.20)$$

and the decomposed jacobian matrix \mathbf{J}' is calculated as

$$\mathbf{J}' := \begin{pmatrix} p_{11} & p_{21} & p_{12} & p_{22} & p_{13} & p_{23} \end{pmatrix}^\top \mathbf{p}_3^\top - \begin{pmatrix} p_{31} & p_{32} & p_{33} \end{pmatrix}^\top \otimes \begin{pmatrix} \mathbf{p}_1 & \mathbf{p}_2 \end{pmatrix}^\top \quad (2.21)$$

in which, \otimes is the kronecker product.

Furthermore,to speed up using matrix-wise calculation, denote a matrix $\mathbf{D} = \begin{pmatrix} \mathbf{d}_1 & \dots & \mathbf{d}_6 \end{pmatrix}^\top \in \mathbb{R}^{6 \times n^3}$:

$$\mathbf{D} := -\frac{2}{n^3} (\mathbf{X}' - f(\tilde{\mathbf{Y}})) \circ (\mathbf{J}' \tilde{\mathbf{Y}}^h) \quad (2.22)$$

in which $\mathbf{X}' = \begin{pmatrix} \mathbf{x}'_1 & \dots & \mathbf{x}'_{n^3} \end{pmatrix}$, \circ is Hadamard product (also known as the Schur product or the entry-wise product) product. Thus, the gradient of S_D with respect to Φ can be expressed by

$$\nabla S_D(\Phi) = \begin{pmatrix} \mathbf{d}_1 + \mathbf{d}_2 & \mathbf{d}_3 + \mathbf{d}_4 & \mathbf{d}_5 + \mathbf{d}_6 \end{pmatrix}^\top \oslash \left((\mathbf{1})_{3 \times 1} (\mathbf{p}_3^\top \tilde{\mathbf{Y}}^h \circ \mathbf{p}_3^\top \tilde{\mathbf{Y}}^h) \right) \quad (2.23)$$

in which \oslash is Hadamard division and $(\mathbf{1})_{3 \times 1}$ is a 3×1 matrix consisting of 1s.

Length Preservation Constraint

The length of one vessel is assumed to be preserved, and thus a strong constraint of length preserving of each edge [35][36] is formulated as:

$$S_L = \frac{1}{n^3} \sum_{i=1}^{n^3} \sum_{j=1}^{\deg(v_i)} \left(\frac{\tilde{l}_{i,j} - l_{i,j}}{l_{i,j}} \right)^2 \quad (2.24)$$

in which, $l_{i,j} = \|\mathbf{y}_i - \mathbf{y}_{\text{ind}(i,j)}\|_2$ is the original length of the j^{th} edge of the i^{th} node, and $\tilde{l}_{i,j} = \|\tilde{\mathbf{y}}_i - \tilde{\mathbf{y}}_{\text{ind}(i,j)}\|_2$ is the deformed length of the j^{th} edge of the i^{th} node. $\text{ind}(i, j)$ return the index of j^{th} adjacent node of the i^{th} node on the 3D skeleton.

The derivative of S_L with respect to φ_i [35] is given by:

$$\frac{\partial S_L}{\partial \varphi_i} = \frac{1}{n^3} \sum_{j=1}^{\deg(v_i)} \frac{2(\tilde{l}_{i,j} - l_{i,j})}{(l_{i,j})^2 \tilde{l}_{i,j}} (\tilde{\mathbf{y}}_i - \tilde{\mathbf{y}}_{\text{ind}(i,j)}) \quad (2.25)$$

Smoothness Constraint

The adjacent nodes for each node of the skeleton graph are assumed to move coherently [36]. Thus, the constraint term of smoothness [36] is calculated as:

$$S_S = \frac{1}{n^3} \sum_{i=1}^{n^3} \sum_{j=1}^{\deg(v_i)} \|\varphi_i - \varphi_{\text{ind}(i,j)}\|^2 \quad (2.26)$$

The derivative of S_S with respect to φ_i [36] is given as:

$$\frac{\partial S_S}{\partial \varphi_i} = \frac{2}{n^3} \sum_{j=1}^{\deg(v_i)} (\varphi_i - \varphi_{\text{ind}(i,j)}) \quad (2.27)$$

Optimization

Using the function *fmincon* in the optimization toolbox (ver. 6.1) of *MATLAB[®]*, multiple optimization algorithms were compared in this non-linear programming problem, including interior algorithm [59], sequential quadratic programming (SQP) algorithm [60] and Broyden-Fletcher-Goldfarb-Shanno (BFGS) method [61]. The BFGS achieved the minimal time consumption and thus was applied in the proposed method.

2.3.5 Post-processing

Thin Plate Spline Warping

After the deformable registration of the assigned nodes of the 3D skeleton, the unassigned nodes of the 3D skeleton are deformed using thin plate spline [62] with the nodes of the connected branches or trunks as the controlling points. It was implemented using the function *TPS3D* from file exchange of *MATLAB[®]*.

2.4 Experiments and Validation

2.4.1 Validation for Segmentation and Reconstruction

The U-Net was trained on the pre-operative CT volumes from different patients. The performance on AAA segmentation was evaluated and compared with varying layers and augmentation methods. The reconstructed AAA shapes were compared with the shape of ground truth.

Dataset

Three pre-operative AAA CTA volumes were collected in a supine position from the celiac trunk to the iliac arteries from different patients. Two of them (Subject 2, Subject 3) scanned by Siemens Definition AS+ were contrast-enhanced while the other one (Subject 1) scanned by Philips ICT 256 was not. The pixel spacing was 0.645~0.977mm and the slice thickness was 0.7~1mm. The AAA in the transverse sectional slices were manually segmented as the ground truth using *Analyze* (*AnalyzeDirect*, Inc, Overland Park, KS, USA). All images were adjusted with a unified pixel spacing of 0.645×0.645 mm by sampling or bilinear interpolation.

Criterion

Dice Similarity Coefficient (DSC) is utilized to evaluate the performance of AAA segmentation in each slice. The equation 2.28 demonstrates the expression.

$$DSC = \frac{2|GT \cap US|}{|GT| + |US|} \quad (2.28)$$

in which, GT is ground truth and US is the segmentation result of U-Net.

2.4.2 Validation for Deformable Registration

To validate the proposed registration approach, multiple experiments were conducted on simulated dataset, phantom dataset and patient dataset. A baseline method [35] was reproduced and compare with the proposed method. Three criteria were used to evaluate the performance on deformable 2D/3D registration of AAA skeletons.

Table 2.1: Trial numbers with the corresponding 3D CT volume and 2D (simulated) fluoroscopic image, respectively indexed by deformation type number

Trial	3D				
	1	2	3	4	5
2D	1	5	9	13	17
	2	1	10	14	18
	3	2	6	15	19
	4	3	7	11	20
	5	4	8	12	16

Datasets

Patient Data Experiment: Fluoroscopic images of the frontal plane and CT volumes from four patients scanned by Siemens CT VA1 Dummy (*Siemens*[®], Pic) were utilized in the experiments, which were contrast-enhanced. The pixel spacing for CT was $0.734 \sim 0.977\text{mm}$ and the slice thickness was 1mm. The pixel spacing of the fluoroscopic images had not been recorded. Four trials of deformable registration were conducted on the four pairs of fluoroscopic image and the corresponding CT volume. However, the deformation type of AAA in each fluoroscopic image is different from that in the CT volume. Thus the ground truth of 3D intra-operative skeletons for the patient data are unavailable.

Phantom Data Experiment: Phantom was also used in the experiments as shown in the fig.2.6. Five types of deformation were made using a string as shown in the fig.2.7. 500mg contrast dose combined with 7L water was pumped into the phantom to simulate the blood circulation of one body. Fluoroscopic images of the frontal plane and CT volumes for the five deformation types were scanned by GE Innova 4100 (*GeneralElectric*[®] Healthcare, Bucks, UK) with the hydraulic pressure of 100mmHg and 70mmHg respectively. The pixel spacing for CT was 0.453mm and the slice thickness was 1mm. The pixel spacing of the fluoroscopic images was 0.507mm. 20 trials were conducted between the fluoroscopic images and the CT volumes with different deformation types, of which the correspondence between

each trial and the fluoroscopic image and CT volume are illustrated in the table 2.1.

Simulated Data Experiment: To evaluate specifically the performance of non-registration of 2D/3D skeletons, the accumulated errors introduced from the stages of segmentation and skeletonization are required to be removed. Thus, the AAAs from the phantom CT volumes were segmented, skeletonized, filtered, and then projected to 2D images of the frontal plane to simulate the skeletons from the fluoroscopic images. 20 trials were conducted between the simulated 2D skeletons and the CT volumes with different deformation types, of which the correspondence between each trial and the fluoroscopic image and CT volume are illustrated in the table 2.1. In addition, five trials for translation testing and five more for rotation testing were conducted between the simulated 2D skeletons and the 3D skeletons translated and rotated based on the initial alignment. Because in the FEVAR, the transformation between X ray machine and the operation table can be directly obtained, we just put the emphasis on the rotation and translation of AAA along the operation table plane, which is usually parallel to the projection plane.



Figure 2.6: Experiments on a phantom, with a pumper simulating the blood circulation



Figure 2.7: Deformation of a phantom, using a string

Criteria

To evaluate the performance in 2D/3D registration of AAA skeletons, three criteria were used including the 2D point-to-curve distance error, the 3D point-to-curve distance error, and the inlier ratio (IR) [63]. The evaluations of 2D and 3D point-to-curve distance error are implemented using the function *distance2curve* from the file exchange of *MATLAB[®]*, and the evaluation of inlier ratio was reproduced according to the description of the "number of inliers" in [63].

2D point-to-curve distance error: The 2D intra-operative skeletons from the fluoroscopic images are the ground truth for the patient data experiments and the phantom data experiments. The simulated 2D intra-operative skeletons using the projected 3D skeletons from phantom CT volumes are the ground truth for the simulated data experiments. A parametric spline approximation is used to fit the curves of the 2D ground truth skeleton. The minimum distance from each point of the projected 3D deformed skeleton to the curve was calculated as the 2D distance error.

3D point-to-curve distance error: The 3D skeletons from CT volumes with the same deformation type as the 2D intra-operative skeletons are regarded as the ground truth for the experiments. A parametric spline approximation is used to fit the curves of the 3D ground truth skeleton. The minimum distance from each point of the 3D

deformed skeleton to the curve was calculated as the 3D distance error.

Inlier Ratio: As described in [63], inlier ratio is the proportion of the inlier assigned 2D nodes in the assigned 2D nodes.

$$IR = \frac{|\{\mathbf{x}' | \exists \text{assigned } \mathbf{y}, \|\mathbf{x}' - f(\mathbf{y})\|_2 \leq \lambda^{-\frac{1}{2}}\}|}{|\{\mathbf{x}'\}|} \quad (2.29)$$

in which, λ is set as 0.25 in the experiments.

Parameter Setting

The branch preserved number τ is set as 5 in the registration of AAA skeletons. The index number tangent vector starting node is set as 1 and the index number tangent vector terminating node is set as 10. The coefficient of length preservation term α is set as 500 and the coefficient of smoothness constraint term β is set as 10.

Baseline Method

The deformable 2D/3D registration approach of vascular structure proposed in [35] applied iterative closest point (ICP) to 2D/3D graph point correspondence, of which the energy function includes difference measure, length preservation constraint, and diffusion regularization using the thin plate spline (TPS) model [35]. It was reproduced as the baseline (ICP-TPS). The coefficient of length preservation term α is set as 0.01, the value of β_{final} is set as 3×10^{-7} , T_{init} is set as 500, T_{final} is set as 1 and T_{update} is set as 0.93 [35]. Since the baseline method is reproduced in *MATLAB* according to [35], some details might be missed affecting on the performance of the algorithm.

Chapter 3

Results

3.1 Segmentation and Reconstruction Results

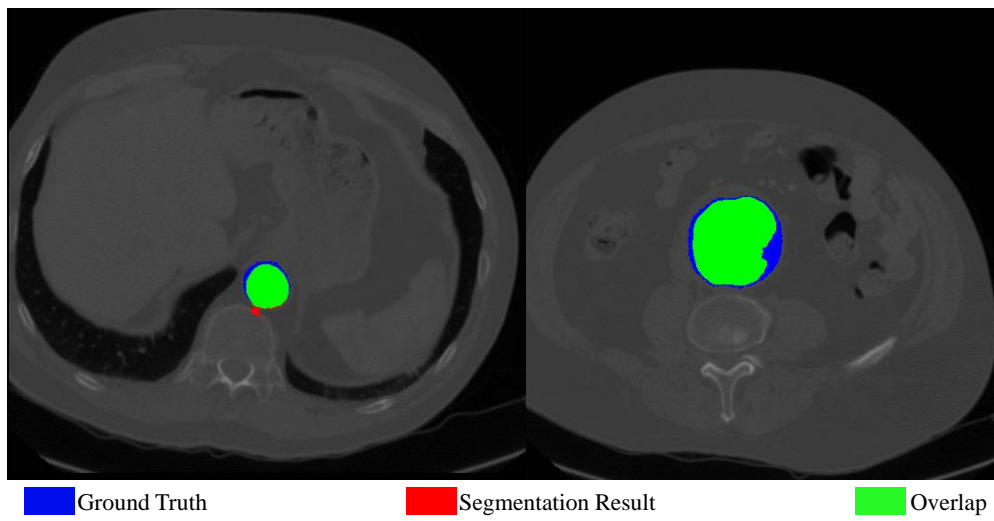


Figure 3.1: Two segmentation examples in different slices of AAA

The U-Net was trained on different two subjects, with varying layers and augmentation methods. As described in equation 2.28, the corresponding DSCs are shown in table 3.1.

In the table 3.1, row 1 and row 2 illustrate that the proposed data augmentation with gray value variation and translation (G.&T.) outperformed the augmentation

combination rotation and mirroring (R.&M.); row 2 and row 3 show that a 34-layer U-Net achieved a higher DSC than a 28-layer U-Net; row 3 and row 4 verify the robustness of the proposed method to variable training subjects and different testing subjects using cross-validation.

Table 3.1: DSCs of AAA segmentation with cross-validation, different data augmentation, and U-Net with varying layers (Num.-Number).

Row	Train Subject	Test Subject	Augmentation	Layer Num.	DSC (avg. \pm std)
1	1, 2	3	R.&M.	34	0.500 ± 0.304
2	1, 2	3	G.&T.	28	0.757 ± 0.151
3	1, 2	3	G.&T.	34	0.802 ± 0.157
4	1, 3	2	G.&T.	34	0.824 ± 0.131

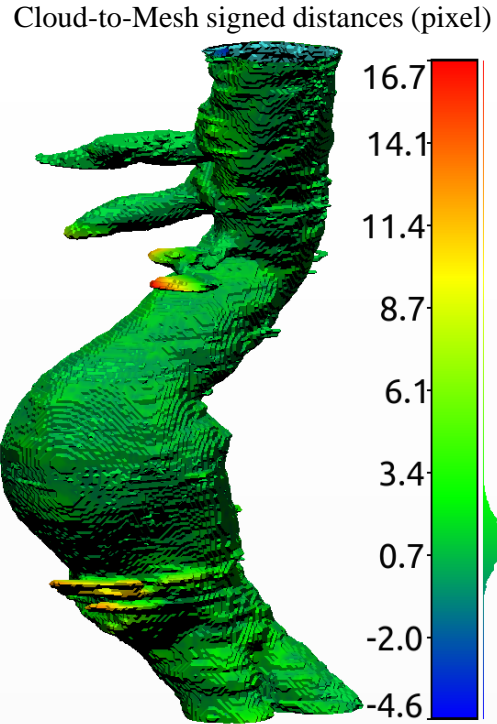


Figure 3.2: A 3D AAA shape, with the colours showing the point cloud-to-mesh distances (unit: pixel) between the model and the ground truth calculated using iterative closest point, and a histogram of distance distribution.

A segmentation example is demonstrated in Fig. 3.1, and a 3D reconstruction result is illustrated in Fig. 3.2, showing that the proximal landing zone, distal landing zone and the aorta are all reconstructed reasonably and the point cloud-to-mesh distances from the segmented shape to the ground truth mesh are distributed around 1 pixels.

However, the renal arteries are not segmented successfully, which is required to be corrected manually.

3.2 Deformable Registration Results

The proposed method and the baseline method of deformable 2D/3D registration [35] were compared through the experiments on the AAA skeletons of different datasets including 30 trials on the simulated data, 20 trials on the phantom data, as well as 4 trials on the patient data.

3.2.1 Simulated Data Experiment

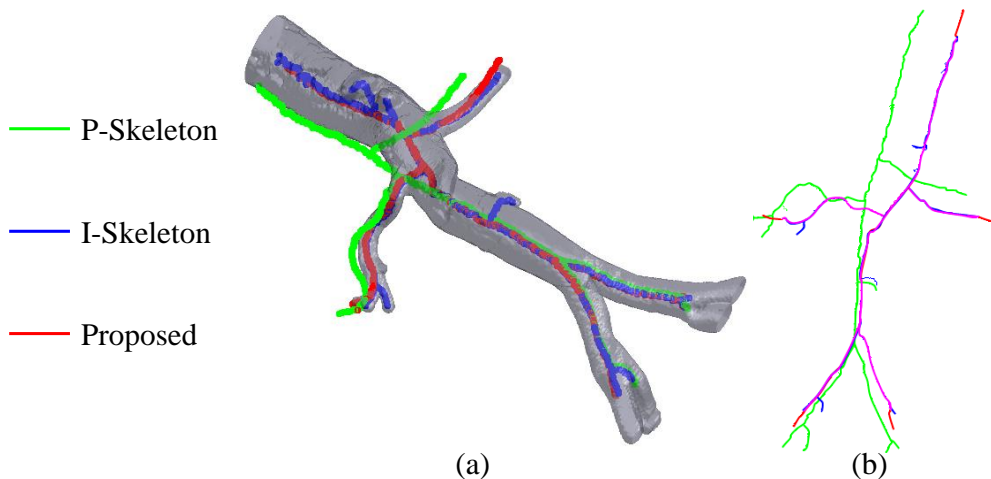


Figure 3.3: One example of deformable registration of AAA on the simulated dataset, in which the green skeleton represents the pre-operative skeleton (P-Skeleton), the blue one represents the intra-operative skeleton (I-Skeleton) as the ground truth and the red one is the deformed skeleton using the proposed method; (a) the deformation registration result in 3D with the semitransparent shape of AAA; (b) the deformation registration result in the 2D projection plane.

Fig.3.3 demonstrates an example of deformable registration of AAA on the simulated dataset in 2D and 3D using the proposed method. The most area of the deformable skeleton and the intra-operative skeleton (ground truth) is overlapped as shown in the 2D projection plane. The results are shown in the table 2 and plotted in fig.3.4,

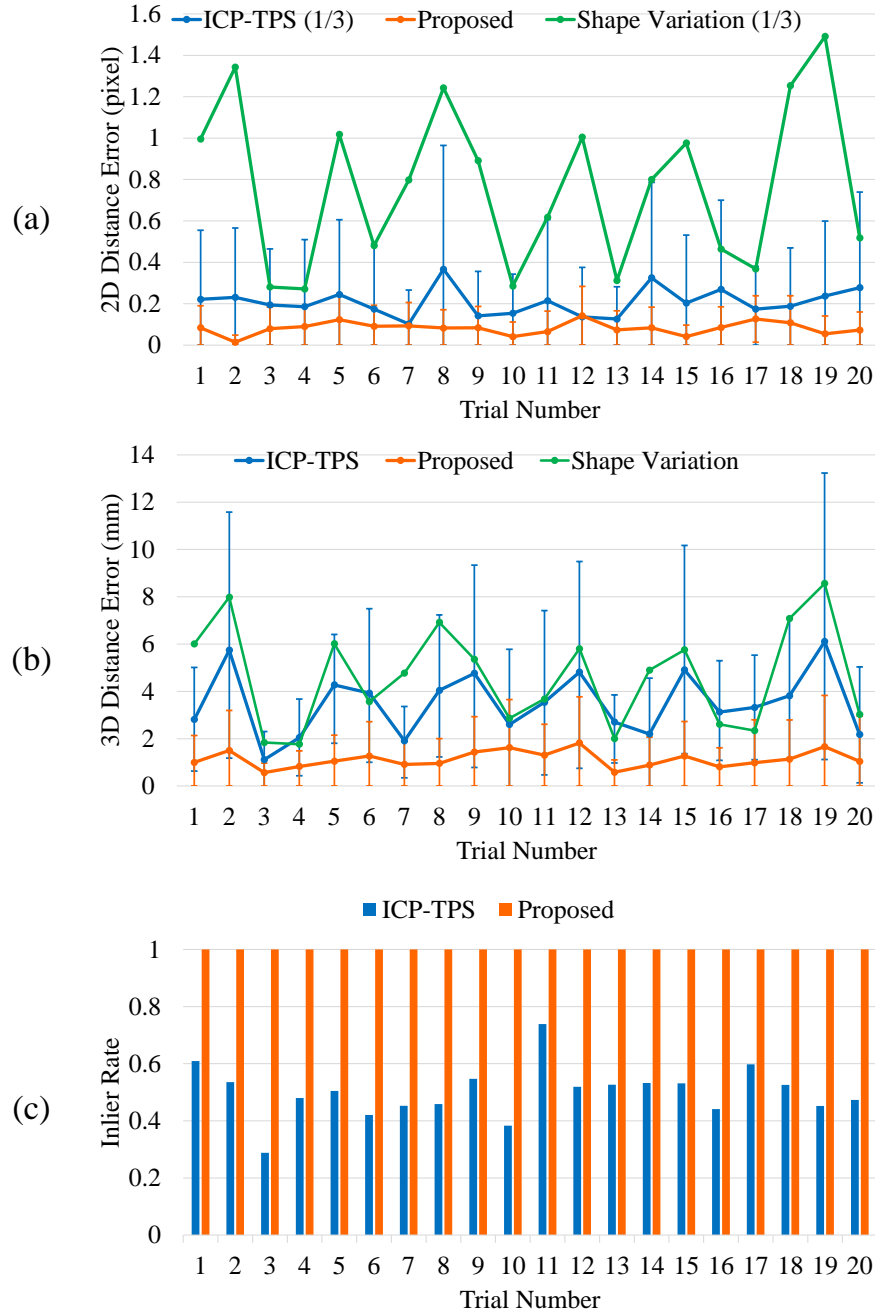


Figure 3.4: Line charts of the 2D and the 3D point-to-curve distance errors (2D and 3D Distance Error) and bar chart of the inlier ratios of the deformable registration of AAA on the 20 trials of simulated dataset; (a) the 2D Distance error distribution, with the green line showing the one third of the shape deformation's error between the ground truth skeletons and the simulated pre-operative skeletons, the blue line showing the one third of the baseline method's error, and the orange line represents the proposed method; (b) the 3D Distance error distribution, with the green line represents the shape deformation between the ground truth skeleton and the pre-operative skeletons, the blue line represents the baseline method, and the orange line represents the proposed method; (c) the inlier ratio (IR): the blue bars showing the IRs of the baseline method, and the orange bars showing the IRs of the proposed method.

including 2D point-to-curve distance errors, 3D point-to-curve distance errors and inlier ratios for the baseline method [35] and the proposed method in the 20 trials with the different pairs of simulated 2D intra-operative skeleton and the 3D skeleton from phantom CT. As shown in the fig.3.4, the average 2D distance error of the proposed method is 0.0817 pixels, the average 3D distance error is 1.1323mm, and the inlier ratio is stable at 1, which are 0.6247 pixels, 2.7600mm and 50.21% for the baseline method [35]. They illustrate that the proposed method is relatively accurate and robust to the varying trial subjects on the simulated dataset. The results of inlier ratio implies that the criterion with the parameter setting is insufficient to evaluate the performance of the proposed method on the simulated dataset.

Rotation testing

Table 3.2: Deformable registration results for a 2D/3D pair of simulated dataset with a varying rotation angle (Angle) in the projection plane which is also the frontal plane of the phantom, including the 2D point-to-curve distance error (2D dist.) and the inlier ratio (IR), comparing the baseline method (ICP-TPS) and the proposed method with the shape variation between the pre-operative skeleton (P-Skeleton) and the ground truth skeleton.

Angle (180°)	Method	2D dist. (pixel)		3D dist. (mm)		IR (%)
		avg.	std.	avg.	std.	
0	P-Skeleton	3.7275	-	6.9198	-	-
	ICP-TPS	1.0990	1.7072	2.8101	3.1943	45.88
	Proposed	0.0824	0.0883	0.9590	1.0441	100.00
0.05	P-Skeleton	3.0527	-	6.4174	-	-
	ICP-TPS	1.4979	1.7424	2.9537	1.8264	32.70
	Proposed	0.0822	0.0876	0.9590	1.0439	100.00
0.1	P-Skeleton	3.1378	-	7.0441	-	-
	ICP-TPS	0.7207	0.9335	3.1037	2.2072	36.07
	Proposed	0.0810	0.0828	0.9591	1.0442	100.00
0.15	P-Skeleton	4.9463	-	10.2839	-	-
	ICP-TPS	1.3414	1.8871	4.5892	3.3000	25.35
	Proposed	0.0813	0.0893	0.9593	1.0420	100.00
0.2	P-Skeleton	7.9419	-	15.5508	-	-
	ICP-TPS	0.6529	1.0758	5.6363	4.4681	49.18
	Proposed	0.0808	0.0868	0.9588	1.0319	100.00

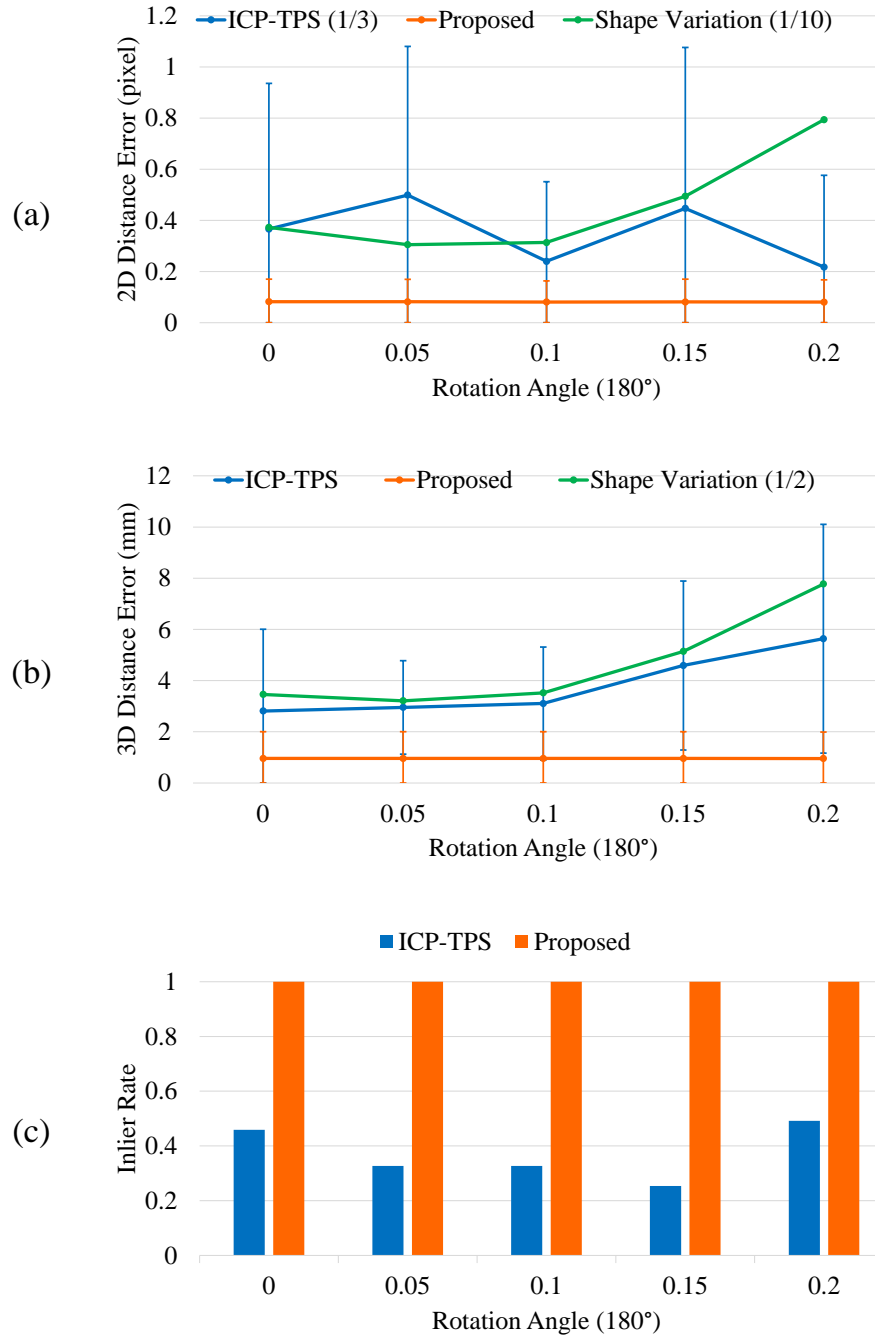


Figure 3.5: Line charts of the 2D and the 3D point-to-curve distance errors (2D and 3D Distance Error) and bar chart of the inlier ratios of the deformable registration of AAA on one simulated subject with varying rotation angle; (a) the 2D Distance error distribution with the green line showing the one tenth of the shape deformation's error between the ground truth skeletons and the simulated pre-operative skeletons, the blue line showing the one third of the baseline method's error, and the orange line showing the errors of the proposed method; (b) the 3D Distance error distribution with the green line showing one half of the shape deformation's error between the ground truth skeletons and the pre-operative skeletons, the blue line showing the baseline method's error, and the orange line represents the proposed method; (c) the inlier ratio (IR): the blue bars showing the IRs of the baseline method, and the orange bars showing the IRs of the proposed method.

As described in the section 2.4.2, the 3D pre-operative skeletons were rotated around the sagittal axis after the pre-alignment to the 2D ground truth (intra-operative) skeleton as the initial position for the deformable registration to test the robustness to rotation around the sagittal axis. The rotation angle varied from 0° to 36° with the resolution of 9° .

The results are shown in the table 3.2 and plotted in fig.3.5, including 2D point-to-curve distance errors, 3D point-to-curve distance errors and inlier ratios of the baseline method [35] and the proposed method. As shown in the fig. 3.5, the average 2D distance error is stable around 0.08 pixels for the proposed method and ranges from 0.6529 to 1.4979; the 3D distance error is stable around 0.96 mm for the proposed method and increases from 2.8101mm to 5.6363mm; and the inlier ratio is stable at 1 for the proposed method and ranges from 25.35 to 45.88. They show that the proposed method is robust to the varying rotation around the sagittal axis.

Translation testing

To test the robustness to translation along the frontal plane, the 3D pre-operative skeletons were translated along the longitudinal axis after the pre-alignment to the 2D ground truth (intra-operative) skeleton as the initial position for the deformable registration. The translation distance varied from 0 unit to 0.2 units with the resolution of 0.05 units, where the 1 unit is the size of one image in the longitudinal axis.

The results are shown in the table 3.3 and plotted in fig.3.6, including 2D point-to-curve distance errors, 3D point-to-curve distance errors and inlier ratios of the baseline method [35] and the proposed method. As shown in the fig.3.6, the average 2D distance error is stable around 0.083 pixels for the proposed method and increases from 1.099 pixels to 1.4523 pixels; the average 3D distance error is stable

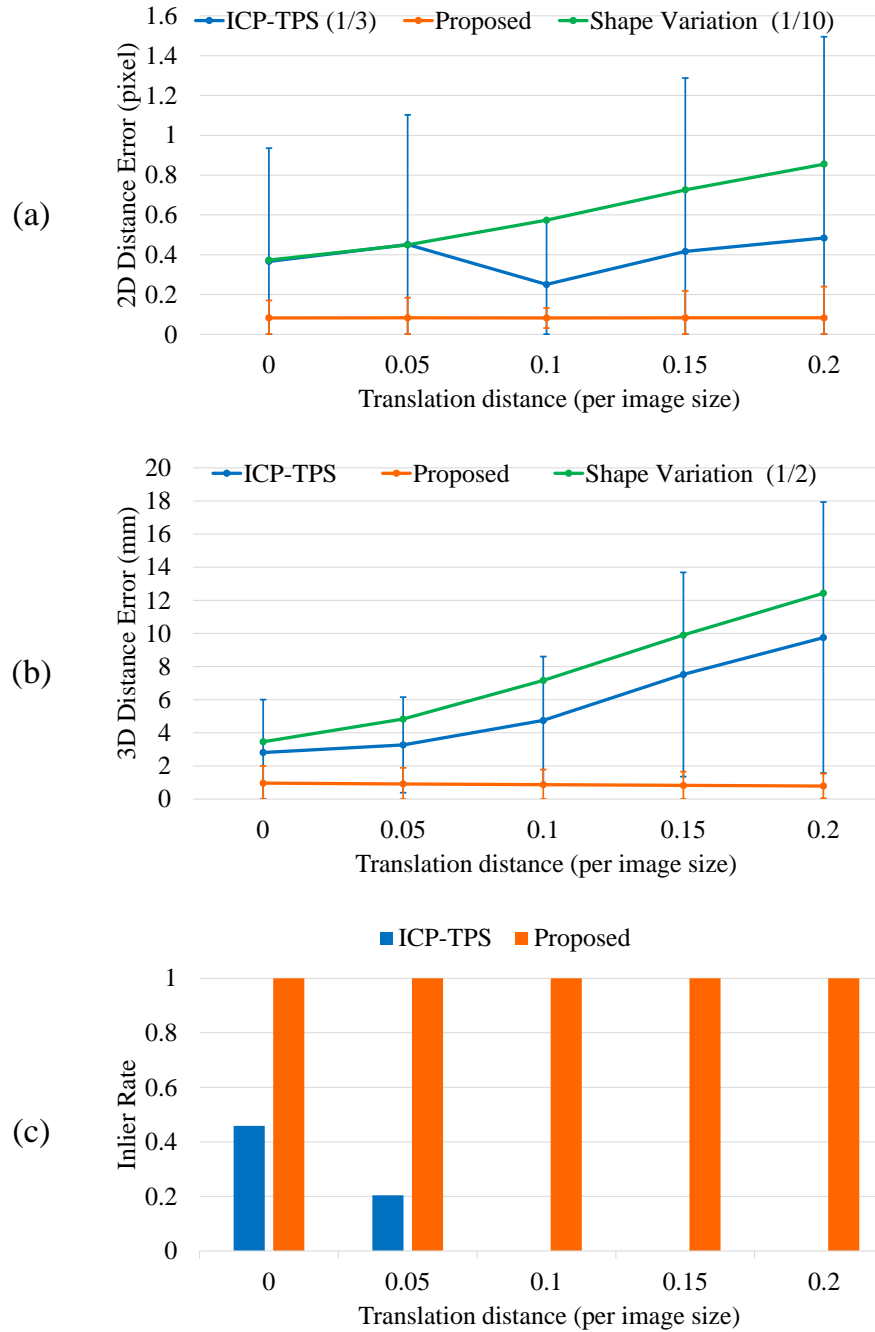


Figure 3.6: Line charts of the 2D and the 3D point-to-curve distance errors (2D and 3D Distance Error) and bar chart of the inlier ratios of the deformable registration of AAA on one simulated subject with varying translation distance; (a) the 2D Distance error distribution with the green line showing the one tenth of the shape deformation's error between the ground truth skeletons and the simulated pre-operative skeletons, the blue line showing the one third of the baseline method's error, and the orange line showing the errors of the proposed method; (b) the 3D Distance error distribution with the green line showing one half of the shape deformation's error between the ground truth skeletons and the pre-operative skeletons, the blue line showing the baseline method's error, and the orange line represents the proposed method; (c) the inlier ratio (IR): the blue bars showing the IRs of the baseline method, and the orange bars showing the IRs of the proposed method.

Table 3.3: Deformable registration results for a 2D/3D pair of simulated dataset with a varying translation distance (Trans.) parallel to the projection plane which is also the frontal plane of the phantom, including the 2D point-to-curve distance error (2D dist.) and the inlier ratio (IR), comparing the baseline method (ICP-TPS) and the proposed method with the shape variation between the pre-operative skeleton (P-Skeleton) and the ground truth skeleton.

Trans. (image size)	Method	2D dist. (pixel)		3D dist. (mm)		IR (%)
		avg.	std.	avg.	std.	
0	P-Skeleton	3.7275	-	6.9198	-	-
	ICP-TPS	1.0990	1.7072	2.8101	3.1943	45.88
	Proposed	0.0824	0.0883	0.9590	1.0441	100.00
0.05	P-Skeleton	4.4922	-	9.6640	-	-
	ICP-TPS	1.3535	1.9564	3.2679	2.8803	20.41
	Proposed	0.0828	1.1012	0.9127	0.9737	100.00
0.1	P-Skeleton	5.7359	-	14.3227	-	-
	ICP-TPS	0.7511	0.9775	4.7487	3.8531	0.00
	Proposed	0.0820	0.0506	0.8690	0.9076	100.00
0.15	P-Skeleton	7.2596	-	19.8003	-	-
	ICP-TPS	1.2493	2.6148	7.5198	6.1674	0.00
	Proposed	0.0825	0.1352	0.8246	0.8359	100.00
0.2	P-Skeleton	8.5539	-	24.8615	-	-
	ICP-TPS	1.4523	3.0340	9.7526	8.1838	0.00
	Proposed	0.0830	0.1569	0.7885	0.7536	100.00

around 0.9 mm for the proposed method and increases from 2.8101 mm to 9.7526 mm. They illustrate that the proposed method is robust to the varying translation along the longitudinal axis. In addition, it is noteworthy that the inlier ratios of the baseline method [35] with the translation distance greater than 0.05 units are equal to 0. There are two potential reasons for this phenomenon. The first one is the term of diffusion regularization limit the deformation of the 3D skeleton, and the correspondence by iterative closest point results in the relatively higher sensitivity to the initial position.

3.2.2 Phantom Data Experiment

Fig.3.7 demonstrates an example of deformable registration of AAA on the phantom dataset in 2D and 3D using the proposed method. The most area of the deformable

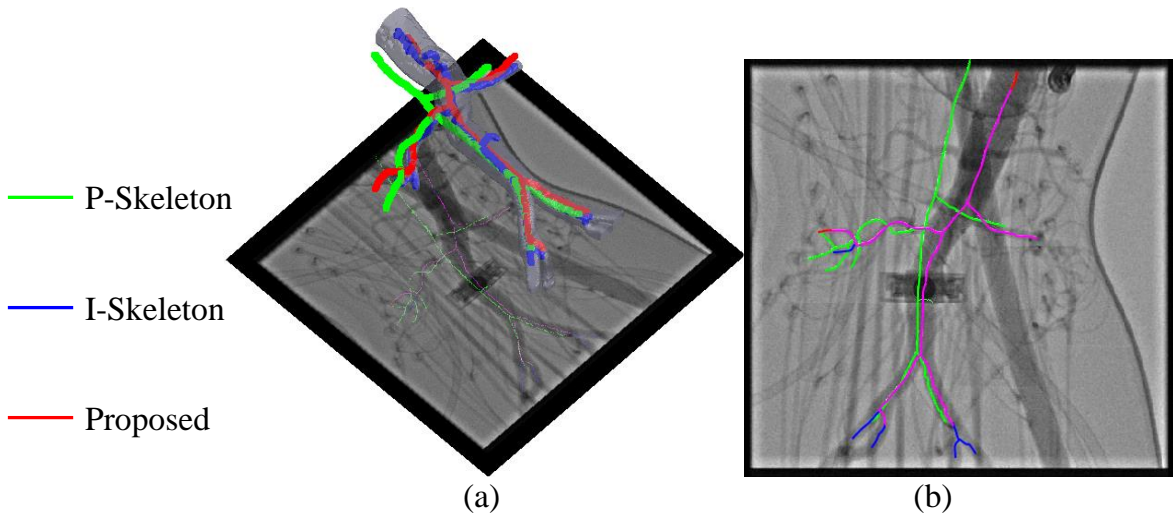


Figure 3.7: One example of deformable registration of AAA on the phantom dataset, in which the green skeleton represents the pre-operative skeleton (P-Skeleton), the blue one represents the intra-operative skeleton (I-Skeleton) as the ground truth, and the red one is the deformed skeleton using the proposed method; (a) the deformation registration result in 3D and 2D with the semitransparent shape of AAA; (b) the deformation registration result in the 2D projection plane.

skeleton and the ground truth skeleton are overlapped, as shown in the 2D projection plane. The quantified results are shown in the table 3 and plotted in fig.3.8, including 2D point-to-curve distance errors, 3D point-to-curve distance errors and inlier ratios of the baseline method and the proposed method for the 20 trials with the different pairs of a 2D intra-operative skeleton from one phantom's fluoroscopic image and a 3D skeleton from the corresponding phantom's CT volumes.

As shown in the fig.3.8, the average 2D distance error is around 0.12 pixels for the proposed method and ranges from 0.3385 pixels to 2.3853 pixels; the inlier ratio is stable at 1 for the proposed method and ranges from 33.83% to 78.07% for the baseline method. It is shown that the average 3D distance error for the proposed method is 2.0180 mm, about 1 mm higher than the result of the simulated data experiment, while that for the baseline method is 3.2949, with the increase of about 0.5 mm comparing with the result of the simulated experiment. It is potentially caused by the deviations between one 2D ground truth skeleton and the corresponding projected 3D ground truth skeleton introduced by the error of segmentation and skeletoniza-

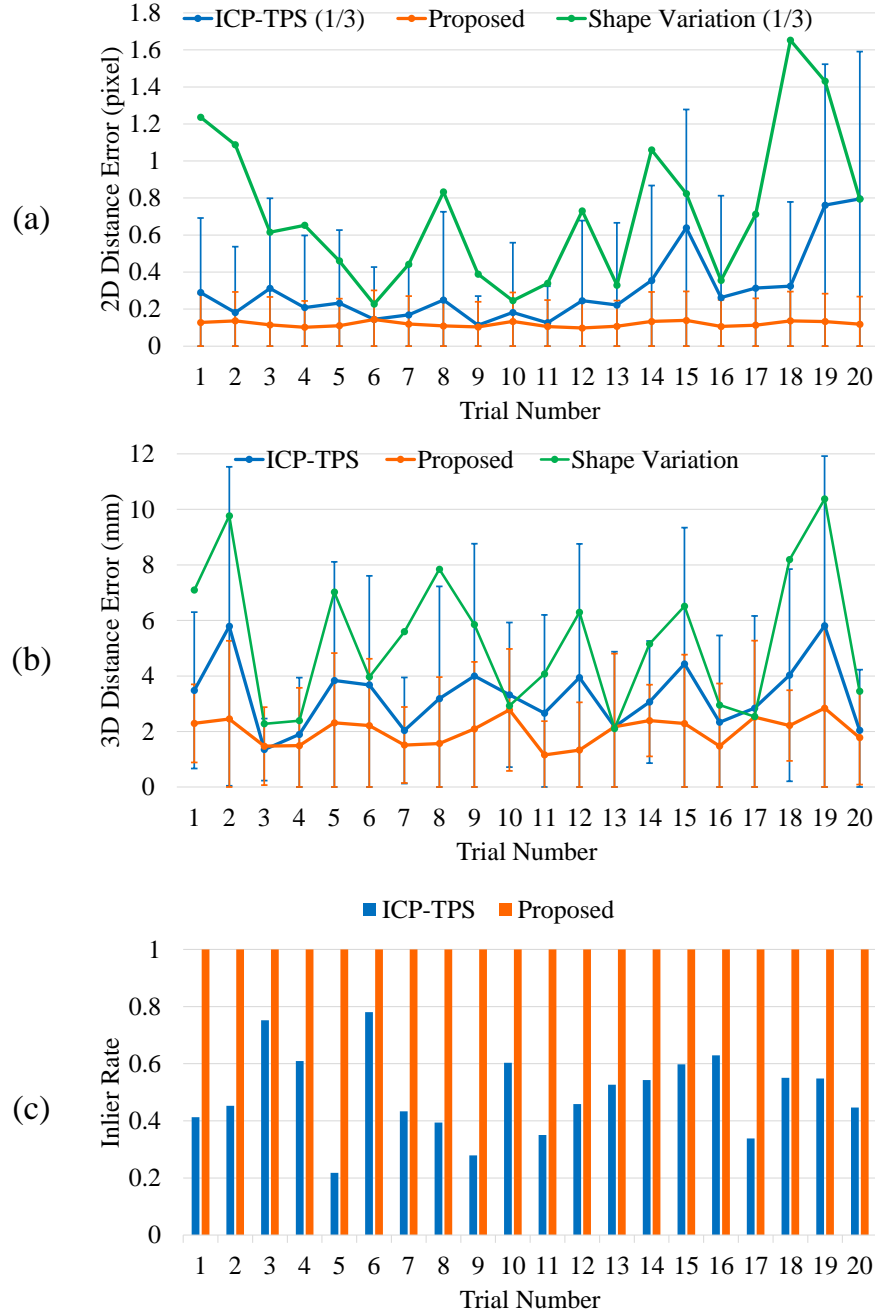


Figure 3.8: Line charts of the 2D and the 3D point-to-curve distance errors (2D and 3D Distance Error) and bar chart of the inlier ratios of the deformable registration of AAA on the 20 trials of phantom dataset; (a) the 2D Distance error distribution with the green line showing the one third error of the shape deformation between the ground truth skeleton and the pre-operative skeletons, the blue line showing the one third error of the baseline method, and the orange line showing the error of the proposed method; (b) the 3D Distance error distribution with the green line showing the shape deformation between the ground truth skeleton and the pre-operative skeletons, the blue line showing the error of the baseline method, and the orange line showing the error of the proposed method; (c) the inlier ratio (IR): the blue bars showing the IRs of the baseline method, and the orange bars showing the IRs of the proposed method.

tion, and the phantom movement and deformation during data collection. According to the results of the three criteria, the proposed method still outperform the baseline method on the phantom dataset. However, the gap is narrowed referring to the results on the simulated dataset. In addition, the results of inlier ratio implies that the criterion with the parameter setting is insufficient to evaluate the performance of the proposed method on the simulated dataset.

3.2.3 Patient Data Experiment

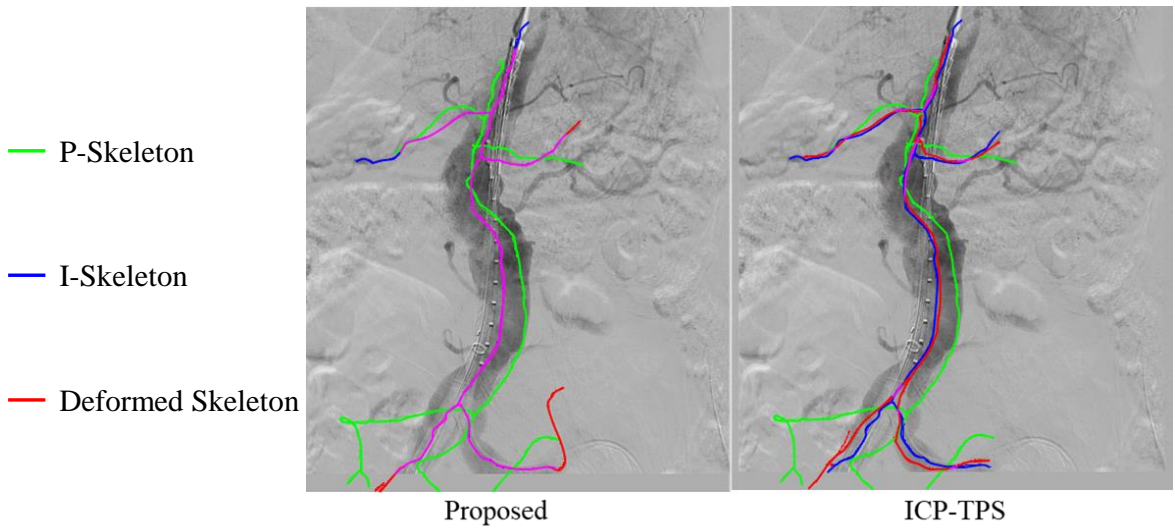


Figure 3.9: One example of deformable registration of AAA on the patient dataset, in which the green skeleton represents the pre-operative skeleton (P-Skeleton), the blue one represents the intra-operative skeleton (I-Skeleton) as the ground truth, and the red one is the deformed skeleton using the proposed method and the baseline method (ICP-TPS); the left picture shows the deformation registration result in the 2D projection plane using the proposed method; the right picture illustrates the deformation registration result in the 2D projection plane using the baseline method.

As described in section 2.4.2, no 3D ground truth skeleton is available in the patient data experiment, and thus only the two criteria, 2D point-to-curve distance error and inlier ratio, can be utilized to evaluate the performance of deformable registration. Fig. 3.9 demonstrates an example of deformable registration of AAA on the patient dataset comparing the proposed method with the baseline method [35], in which the skeletons' deformations are larger than in the phantom data experiment,

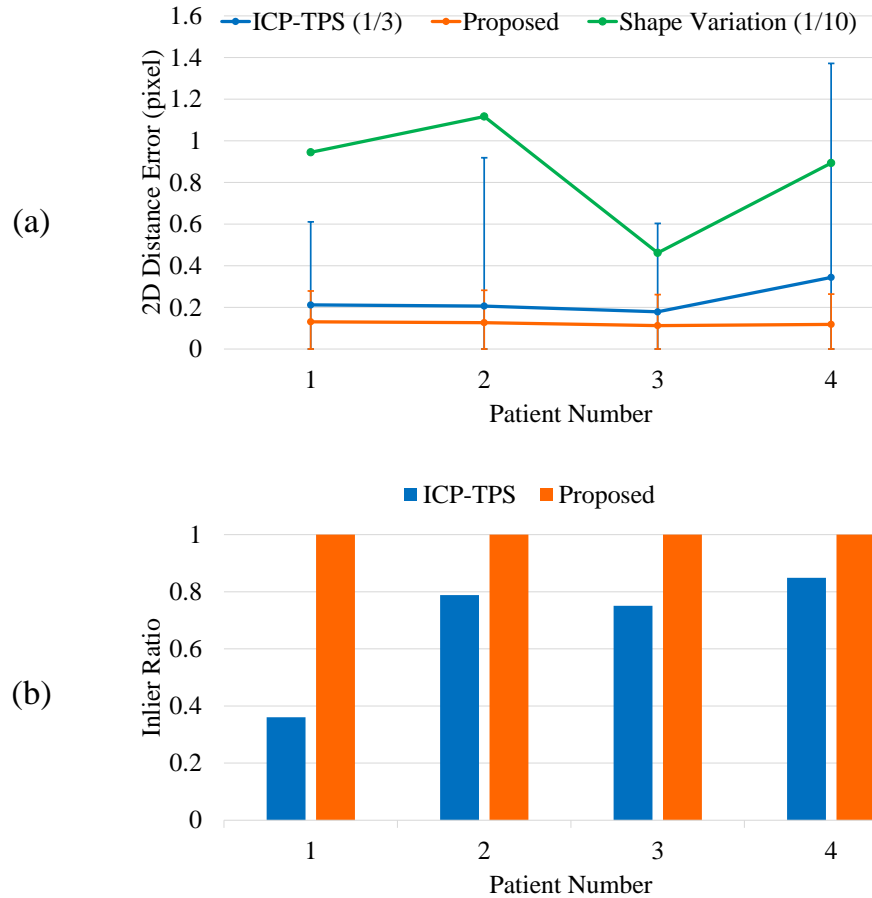


Figure 3.10: Line chart of the 2D point-to-curve distance errors (2D Distance Error) and bar chart of the inlier ratios of the deformable registration of AAA on the four patients' data; (a) the 2D Distance error distribution with the green line showing the one tenth error of the shape deformation between the ground truth skeleton and the pre-operative skeletons, the blue line showing the one third error of the baseline method, and the orange line showing the error of the proposed method; (b) the inlier ratio (IR): the blue bars showing the IRs of the baseline method, and the orange bars showing the IRs of the proposed method.

Table 3.4: Deformable registration results for the four patient data experiments, including the 2D point-to-curve distance error (2D dist.) and the inlier ratio (IR), comparing the baseline method (ICP-TPS) and the proposed method with the shape variation between the pre-operative skeleton (P-Skeleton) and the ground truth skeleton

Patient	Method	2D dist. (pixel)		IR (%)
		avg.	std.	
1	P-Skeleton	9.4509	-	-
	ICP-TPS	0.6357	1.1966	36.07
	Proposed	0.1309	0.1482	100.00
2	P-Skeleton	11.1678	-	-
	ICP-TPS	0.6200	2.1370	78.86
	Proposed	0.1268	0.1554	100.00
3	P-Skeleton	4.6217	-	-
	ICP-TPS	0.5364	1.2741	75.11
	Proposed	0.1127	0.1488	100.00
4	P-Skeleton	8.9363	-	-
	ICP-TPS	1.0325	3.0812	84.92
	Proposed	0.1185	0.1455	100.00

but the deformations are recovered well according to the intuitive results of the 2D projection plane.

The quantified results are shown in the table 3.4 and plotted in fig. 3.10, including 2D point-to-curve distance errors and inlier ratios of the baseline method and the proposed method for the experiment on four pairs of one 2D intra-operative skeleton from a patient's fluoroscopic images and the 3D skeleton from the pre-operative CT volume of the same patient. As shown in the fig. 3.10, the average 2D distance error is around 0.12 pixels for the proposed method and ranges from 0.5364 pixels to 1.0325 pixels; the inlier ratio is stable at 1 for the proposed method and ranges from 36.07% to 84.92% for the baseline method, which are roughly consistent with the results of the simulated data experiment and the phantom data experiment. According to these results of the two criteria, the proposed method performs better than the baseline method on the patient dataset.

Chapter 4

Discussion

4.1 Performance Analysis

4.1.1 Accuracy

According to the results shown in the chapter 3, the average DSC of 0.81 was achieved in the segmentation of AAA from patients' CT volume and reasonable shapes of AAA are reconstructed. However, it was observed in the result of subject 2 and subject 3 that the segmentation and reconstruction accuracy in the regions of iliac arteries and renal arteries are less than the others, which potentially causes the structure variation of the AAA. One solution is to segment these regions using

Table 4.1: Deviation between the 2D ground truth skeleton and the 2D projection of the corresponding 3D ground truth skeleton for the five deformation types on the phantom data quantified by the 2D point-to-curve distance error (2D dist.).

Deformation Type	2D dist. (pixel)	
	avg.	std.
1	1.6518	3.6366
2	0.6676	0.9654
3	0.5133	0.9147
4	0.5711	0.9384
5	0.9041	2.3141

other methods. In this project, intensity threshold and region growing implemented in *ITK-SNAP* were also utilized to improve the segmentation.

The average 2D point-to-curve distance error of 0.0817 pixels and the average 3D point-to-curve distance error of 1.1323mm were obtained for the proposed method in the deformable registration on the simulated dataset, comparing with the average 2D distance error of 0.6247 pixels and the average 3D distance error of 2.7600mm for the baseline method [35], based on the average 2D distance error of 2.3119 pixels and average 3D distance error of 4.6431mm for the shape deformation of the ground truth. It is a specific evaluation for the deformable registration of skeletons, minimizing the influence of segmentation and skeletonization.

In the experiment of phantom data, the average 2D point-to-curve distance error of the proposed method is 0.1196 pixels, slightly more than the result in simulated data experiment, and smaller than the baseline's 0.9188 pixels. However, the average 3D point-to-curve distance error of the proposed method is increased to 2.0180mm, which almost doubles the result of the simulated data experiment, while the baseline method [35] achieved 3.2949mm. It is potentially caused by the deviations between one 2D ground truth skeleton and the corresponding projected 3D ground truth skeleton introduced by the error of segmentation and skeletonization, and the phantom movement in the process of data collection. The quantified deviations are shown in table 4.1. Referring to the correspondence table 2.1, a positive correlation is found between the deviations of one pair of 2D/3D ground truth skeletons and the increase proportions (compared with the simulated data experiment) of 3D point-to-curve distance for the trials with the corresponding 2D skeleton. The correlation index is 0.3848 for the proposed method and 0.1432 for the baseline method [35].

In the experiment of patient data, the average 2D distance error for the shape deformation of the ground truth skeletons is 8.544 pixels, which shows that the deformation in the patient data is larger than in the simulated data and the phantom

data. The proposed method achieved the average 2D distance error of 0.1222 pixels, comparing with 0.7061 pixels for the baseline method [35].

4.1.2 Runtime

Each step in the process of the 3D robotic path planning can be classified as pre-operative or intra-operative. The pre-operative steps include segmentation, resizing, skeletonization, graph construction and node classification of a 3D AAA. The intra-operative steps includes segmentation, skeletonization, graph construction and node classification of a 2D AAA, as well as the rigid registration (pre-alignment), branch and trunk matching and node assignment between the 2D and 3D AAA skeletons and the iterative optimization of the energy function. The runtime of each step will be discussed, while the efficiency of those intra-operative steps has greater significance for clinical application.

Pre-operative time consumption: In the step of 3D segmentation it takes 8~12 hours for training a DCNN on a 12GB GPU (*NVIDIA[®]* Titan Xp), and the runtime of testing is about 0.1 seconds to automatically segment one slice of CT volume with the size of 512×512 , which was implemented in *python – tensorflow*. After that, the other steps were all implemented in *MATLAB[®]* and executed on a 3.6GHz×8 CPU (*Intel[®]* Core). The resizing and skeletonization [51] of a 3D AAA volume with the size of $512 \times 512 \times L$ totally cost over 3 minutes, in which L is the slice number varying from 200 to 500. The time consumption is $0.1 \sim 0.3$ seconds for the skeleton graph construction followed by the node classification of the 3D skeleton.

Intra-operative time consumption: The average time cost by skeletonization of one 2D AAA from a 512×512 fluoroscopic image is 0.91 seconds. The total time consumption of the intra-operative steps in the deformable 2D/3D skeleton registration for the proposed method is recorded, including the graph construction and node

classification of a 2D skeleton, as well as the branch and trunk matching and node assignment between the 2D and 3D skeletons. The time consumption of the deformable registration step using both the proposed method and the baseline method [35] rely on the number of the used graph nodes. There were $900 \sim 1000$ 2D graph nodes and $900 \sim 1000$ 3D graph nodes used in the simulated data experiment, $700 \sim 900$ 2D graph nodes and $900 \sim 1100$ 3D graph nodes used in the phantom data experiment, and $800 \sim 900$ 2D graph nodes and $700 \sim 1200$ 3D graph nodes used in the phantom data experiment, corresponding to 0.96, 0.84 and 0.78 seconds for the intra-operative step in the part of deformable 2D/3D skeleton registration using the proposed method which is compared with 874.1, 697.4 and 1010.9 seconds for the baseline method [35].

4.1.3 Robustness

The influence of a series of parameters were considered including the rotation and translation after pre-alignment, the topological structure of skeletons, the length of segmented arteries, the shape deformation.

Rotation and translation after pre-alignment: As discussed in the section 2.3, the rigid registration as pre-alignment between the 2D and 3D AAA skeleton has been solved. However, the translation and rotation during the intervention are still noteworthy. The robustness of deformable registration method to rotation and translation might improve the efficiency of the navigation process of FEVAR. In clinical practice, the physical position of the projection plane is usually parallel to the table plane of intervention, and the supine position is common used in FEVAR, which implies that the rotation around the sagittal axis and the translation parallel to the projection plane are the most probable transformation in FEVAR. Thus the emphasis was put on the testing of these transformation in this article. According to [56] and the results shown in the fig. 3.5 and fig. 3.6, the performance of ICP algorithms

heavily relies on the initialization of rigid registration, while the proposed is relatively robust to the translation and rotation parallel to the projection plane.

Lengths of segmented arteries: There are two potential factors about the length of segmented arteries affecting the results of deformable 2D/3D registration. First, the lengths of the same segmented arteries in 2D and 3D might be different, which results in unassigned nodes at 2D or 3D branches. The baseline method [35] uses the ICP and thresholding to detect outliers[35]. It is intuitively observed that a projected 3D branch longer than the corresponding 2D branch causes an unreasonable assignment of the branch nodes in 2D and 3D, and an unnatural deformation on the deformed 3D branch. The potential reason is that the unassigned nodes (called outliers in [35]) are discarded after the softassigning between 2D and 3D skeletons in [35]. The proposed method detects the outliers by comparing the path length of each pair of branches for a 2D skeleton and the projection of a 3D skeleton, which improves the robustness to the difference between the lengths of the same branches from 2D image and projected from 3D. The second one is the length difference between those branches in 2D or 3D. Since the five preserved branches in the proposed method are specified as the two renal arteries, the two iliac arteries and the upper aorta referring to their branch length, the proposed method is sensitive to the length difference between those branches in 2D or 3D. The manual intervention for parameter setting will be required if the length of those segmented arteries are inaptitude.

Shape Deformation: The baseline method [35] uses the thin plate spline to recover and constrain the deformation of the whole graph [35], which has also been used in [48][49][36]. However, the 2D distance error for the baseline method [35] illustrated that the local deformations were limited by the diffusion regularization term according to the results of those experiments, and the coupling deformations were also observed on the unassigned nodes of two nearby branches. The radial basis function used in thin plate spline implies one assumption that the interaction of the

displacement two points at one tissue is only related to the euclidean distance between the two points. However, it is untenable in the global deformation of AAA, which is a potential reason for the problem in the baseline method [35]. Thus, a smoothness constraint term [36] with adjacent information of graph nodes was applied in the energy function of the proposed method replacing the diffusion regularization term, and the unassigned nodes are moved using the branch-wise 3D TPS with the connected branch nodes as the controlling points. According to the results illustrated in the chapter 3, the proposed method is relatively robust to a varying shape deformation comparing with the baseline method [35].

Topological structure of skeletons: As stated and evaluated in the chapter 3 and the previous section, the segmentation of 3D AAA shape achieve a high accuracy in most region except the iliac arteries and renal arteries. This might change the structure of the segmented AAA and thus the topological structure of a 3D skeleton. For example, if one or more iliac or renal arteries are not segmented from one CT volume or an unexpected artery/aorta is segmented much longer than any one of the expected arteries/aorta, the deformable 2D/3D skeleton registration will be failed using the proposed method since it is based on the skeleton graph matching. This problem is solved by semi-automatic method including intensity threshold and region growing implemented in *ITK-SNAP*. In addition, the topological changes of a 2D skeleton results from the intersection between two of the five specified arteries/aorta on the projection plane, which could invalidate the proposed method. This case has not been found among all the dataset we used. Thus, the proposed method has low robustness to the varying topological structure of 2D and 3D skeletons.

4.2 Achievement and Limitation

The one-stage DCNN, U-Net [20] , was applied to the automatical segmentation of AAA shapes from CT volumes. The overfitting caused by the small number of training subjects was solved using data augmentation based on gray value variation and translation for training. Comparing with many training subjects required in previous work [23][24][25], a reasonable DSC result has been achieved using a small number of training subjects. A drawback is that the segmentation and reconstruction accuracy in the regions of iliac arteries and renal arteries are less than the others, which might require manual intervention.

A deformable 2D/3D registration method of AAA skeletons based on graph matching has been proposed. The experiments shows that the proposed method, comparing with the baseline method [35], is more accurate, efficient and robust to the translation and rotation parallel to the projection plane, as well as the shape deformation. However, it is sensitive to the topological change of 2D and 3D skeletons and the length difference between the segmented arteries. In addition, since the baseline method was reproduced according to [35], some details might be missed affecting on the performance of the algorithm. The parameter setting for the baseline method was adjusted to optimize the performance in the experiments based on [35].

Together with the segmentation of AAA from fluoroscopic image and the skeletonization of 2D and 3D AAA [51], the 3D deformation recovering the intra-operative AAA skeleton from a single fluoroscopic image has been achieved as the path for the catheter robot in FEVAR.

4.3 Future work

The segmentation of AAA will be improved in the future to raise the accuracy of deformable 2D/3D registration of AAA skeletons. Batch normalization [64] can be used to improve the performance of DCNN and a fully connected conditional random field [15] can be applied to locating the boundaries of one object. Improvement of the segmentation of AAA will raise the accuracy and robustness of deformable 2D/3D registration of AAA skeletons.

Furthermore, the shape instantiation of AAA from a single fluoroscopic image will be implemented in the future for an accurate navigation of FEVAR and EVAR. Since the 3D deformation of one AAA skeleton has been recovered from a single fluoroscopic image, the mesh manipulation based on skeleton deformation is required for recovering the shape deformation of AAA. A skeleton based morphing was proposed for a sketch based deformation in [65], which could be applied to the mesh manipulation of AAA shape with a deformed skeleton.

4.4 Conclusion

In this article, the literatures related to semantic segmentation, rigid and non-rigid 2D/3D registrations were reviewed. A DCNN architecture was applied to the segmentation of AAA shape. Two combinations of data augmentation and a varying layer number of U-net were compared using the segmentation results. A method for deformable 2D/3D registration of AAA skeletons was proposed, which are described in detail. The graph of 2D and 3D skeletons were constructed and the softassignment of graph nodes was calculated based on the path length to improve the accuracy and efficiency of correspondence between 2D and 3D skeleton nodes. A baseline method of deformable 2D/3D registration [35] was compared with the proposed method

on different datasets with three criteria. These qualitative and quantitative tests demonstrated the improvement achieved in the 3D deformation recovering of the intra-operative AAA skeleton from a single fluoroscopic image.

Bibliography

- [1] B. C. Mendes, G. S. Oderich, M. P. Correa, and K. S. Kanamori, “Endovascular repair of complex aortic pathology,” *Current Surgery Reports*, vol. 1, no. 2, pp. 67–77, 2013. pages 2
- [2] N. Sakalihasan, R. Limet, and O. Defawe, “Abdominal aortic aneurysm,” *The Lancet*, vol. 365, no. 9470, pp. 1577–1589, 2005. pages 2
- [3] K. C. Kent, “Abdominal aortic aneurysms,” *New England Journal of Medicine*, vol. 371, no. 22, pp. 2101–2108, 2014. pages 2, 3
- [4] R. Greenhalgh *et al.*, “Comparison of endovascular aneurysm repair with open repair in patients with abdominal aortic aneurysm (evar trial 1), 30-day operative mortality results: randomised controlled trial,” *The Lancet*, vol. 364, no. 9437, pp. 843–848, 2004. pages 2
- [5] X.-Y. Zhou, J. Lin, C. Riga, G.-Z. Yang, and S.-L. Lee, “Real-time 3D shape instantiation from single fluoroscopy projection for fenestrated stent graft deployment,” *IEEE Robotics and Automation Letters*, 2018. pages 2
- [6] J. Cross, K. Gurusamy, V. Gadhvi, D. Simring, P. Harris, K. Ivancev, and T. Richards, “Fenestrated endovascular aneurysm repair,” *British Journal of Surgery*, vol. 99, no. 2, pp. 152–159, 2012. pages 2, 3
- [7] J. H. Park, J. W. Chung, I. W. Choo, S. J. Kim, J. Y. Lee, and M. C. Han, “Fenestrated stent-grafts for preserving visceral arterial branches in the treatment of abdominal aortic aneurysms: preliminary experience,” *Journal of Vascular and Interventional Radiology*, vol. 7, no. 6, pp. 819–823, 1996. pages 3
- [8] G. A. Antoniou, C. V. Riga, E. K. Mayer, N. J. Cheshire, and C. D. Bicknell, “Clinical applications of robotic technology in vascular and endovascular surgery,” *Journal of vascular surgery*, vol. 53, no. 2, pp. 493–499, 2011. pages 3
- [9] L. W. Klein, D. L. Miller, S. Balter, W. Laskey, D. Haines, A. Norbush, M. A. Mauro, and J. A. Goldstein, “Occupational health hazards in the interventional laboratory: time for a safer environment,” *Heart Rhythm*, vol. 6, no. 3, pp. 439–444, 2009. pages 3
- [10] D. Toth, M. Pfister, A. Maier, M. Kowarschik, and J. Hornegger, “Adaption of 3D models to 2D x-ray images during endovascular abdominal aneurysm repair,”

- in *International Conference on Medical Image Computing and Computer-Assisted Intervention*, pp. 339–346, Springer, 2015. pages 3, 9, 10
- [11] S. Macdonald, R. Lee, R. Williams, G. Stansby, *et al.*, “Towards safer carotid artery stenting: a scoring system for anatomic suitability,” *Stroke*, vol. 40, no. 5, pp. 1698–1703, 2009. pages 3
 - [12] G. Litjens, T. Kooi, B. E. Bejnordi, A. A. A. Setio, F. Ciompi, M. Ghafoorian, J. A. van der Laak, B. van Ginneken, and C. I. Sánchez, “A survey on deep learning in medical image analysis,” *Medical image analysis*, vol. 42, pp. 60–88, 2017. pages 4, 5, 6, 10
 - [13] B. Hariharan, P. Arbeláez, R. Girshick, and J. Malik, “Simultaneous detection and segmentation,” in *European Conference on Computer Vision*, pp. 297–312, Springer, 2014. pages 4
 - [14] R. Girshick, J. Donahue, T. Darrell, and J. Malik, “Rich feature hierarchies for accurate object detection and semantic segmentation,” in *Proceedings of the IEEE conference on computer vision and pattern recognition*, pp. 580–587, 2014. pages 4
 - [15] L.-C. Chen, G. Papandreou, I. Kokkinos, K. Murphy, and A. L. Yuille, “Deeplab: Semantic image segmentation with deep convolutional nets, atrous convolution, and fully connected crfs,” *IEEE transactions on pattern analysis and machine intelligence*, vol. 40, no. 4, pp. 834–848, 2018. pages 4, 6, 59
 - [16] R. Girshick, “Fast r-cnn,” in *Proceedings of the IEEE international conference on computer vision*, pp. 1440–1448, 2015. pages 5
 - [17] S. Ren, K. He, R. Girshick, and J. Sun, “Faster r-cnn: Towards real-time object detection with region proposal networks,” in *Advances in neural information processing systems*, pp. 91–99, 2015. pages 5
 - [18] K. He, G. Gkioxari, P. Dollár, and R. Girshick, “Mask r-cnn,” in *Computer Vision (ICCV), 2017 IEEE International Conference on*, pp. 2980–2988, IEEE, 2017. pages 5
 - [19] J. Long, E. Shelhamer, and T. Darrell, “Fully convolutional networks for semantic segmentation,” in *Proceedings of the IEEE conference on computer vision and pattern recognition*, pp. 3431–3440, 2015. pages 5, 6
 - [20] O. Ronneberger, P. Fischer, and T. Brox, “U-net: Convolutional networks for biomedical image segmentation,” in *International Conference on Medical image computing and computer-assisted intervention*, pp. 234–241, Springer, 2015. pages 6, 13, 58
 - [21] Ö. Çiçek, A. Abdulkadir, S. S. Lienkamp, T. Brox, and O. Ronneberger, “3D u-net: learning dense volumetric segmentation from sparse annotation,” in *International Conference on Medical Image Computing and Computer-Assisted Intervention*, pp. 424–432, Springer, 2016. pages 6

- [22] F. Milletari, N. Navab, and S.-A. Ahmadi, “V-net: Fully convolutional neural networks for volumetric medical image segmentation,” in *3D Vision (3DV), 2016 Fourth International Conference on*, pp. 565–571, IEEE, 2016. pages 6
- [23] H. A. Hong and U. Sheikh, “Automatic detection, segmentation and classification of abdominal aortic aneurysm using deep learning,” in *CSPA*, pp. 242–246, IEEE, 2016. pages 6, 58
- [24] K. López-Linares, L. Kabongo, N. Lete, G. Maclair, M. Ceresa, A. García-Familiar, I. Macía, and M. Á. G. Ballester, “Dcnn-based automatic segmentation and quantification of aortic thrombus volume: Influence of the training approach,” in *CVII-STENT and LABELS workshop in MICCAI*, pp. 29–38, Springer, 2017. pages 6, 58
- [25] K. López-Linares, N. Aranuelo, L. Kabongo, G. Maclair, N. Lete, M. Ceresa, A. García-Familiar, I. Macía, and M. A. G. Ballester, “Fully automatic detection and segmentation of abdominal aortic thrombus in post-operative cta images using deep convolutional neural networks,” in *MedIA*, 2018. pages 6, 7, 58
- [26] B. Zitova and J. Flusser, “Image registration methods: a survey,” *Image and vision computing*, vol. 21, no. 11, pp. 977–1000, 2003. pages 7, 8, 9
- [27] S. Demirci, A. Bigdelou, L. Wang, C. Wachinger, M. Baust, R. Tibrewal, R. Ghotbi, H.-H. Eckstein, and N. Navab, “3D stent recovery from one x-ray projection,” in *International Conference on Medical Image Computing and Computer-Assisted Intervention*, pp. 178–185, Springer, 2011. pages 7
- [28] J. P. Pluim, J. A. Maintz, and M. A. Viergever, “Mutual-information-based registration of medical images: a survey,” *IEEE transactions on medical imaging*, vol. 22, no. 8, pp. 986–1004, 2003. pages 8
- [29] F. E.-Z. A. El-Gamal, M. Elmogy, and A. Atwan, “Current trends in medical image registration and fusion,” *Egyptian Informatics Journal*, vol. 17, no. 1, pp. 99–124, 2016. pages 8, 9
- [30] N. Hanaizumi and S. Fujimur, “An automated method for registration of satellite remote sensing images,” in *Geoscience and Remote Sensing Symposium, 1993. IGARSS'93. Better Understanding of Earth Environment., International*, pp. 1348–1350, IEEE, 1993. pages 8
- [31] D. I. Barnea and H. F. Silverman, “A class of algorithms for fast digital image registration,” *IEEE transactions on Computers*, vol. 100, no. 2, pp. 179–186, 1972. pages 8
- [32] S. Ramachandran, C. Calcagno, V. Mani, P. M. Robson, and Z. A. Fayad, “Registration of dynamic contrast-enhanced mri of the common carotid artery using a fixed-frame template-based squared-difference method,” *Journal of Magnetic Resonance Imaging*, vol. 39, no. 4, pp. 1017–1017, 2014. pages 8

- [33] W. R. Crum, T. Hartkens, and D. Hill, “Non-rigid image registration: theory and practice,” *The British journal of radiology*, vol. 77, no. suppl_2, pp. S140–S153, 2004. pages 8, 9
- [34] J. Kim, J. Lee, J. W. Chung, and Y.-G. Shin, “Locally adaptive 2d–3d registration using vascular structure model for liver catheterization,” *Computers in biology and medicine*, vol. 70, pp. 119–130, 2016. pages 8
- [35] M. Groher, D. Zikic, and N. Navab, “Deformable 2d-3d registration of vascular structures in a one view scenario,” *IEEE Transactions on Medical Imaging*, vol. 28, no. 6, pp. 847–860, 2009. pages 8, 9, 10, 15, 28, 29, 30, 31, 33, 37, 40, 42, 44, 46, 49, 53, 54, 55, 56, 57, 58, 59
- [36] R. Liao, Y. Tan, H. Sundar, M. Pfister, and A. Kamen, “An efficient graph-based deformable 2d/3d registration algorithm with applications for abdominal aortic aneurysm interventions,” in *International Workshop on Medical Imaging and Virtual Reality*, pp. 561–570, Springer, 2010. pages 8, 9, 10, 15, 31, 56, 57
- [37] R. Jumeau, N. Peguret, C. Zulliger, R. Moeckli, J. Bourhis, and E. Ozsahin, “Optimization of reirradiation using deformable registration,” *International Journal of Radiation Oncology Biology Physics*, vol. 93, no. 3, p. E599, 2015. pages 9
- [38] L. Sibille, C. Hutton, and J. Declerck, “Deformable registration for 18f-florbetapir pet quantification,” in *European Journal of Nuclear Medical and Molecular Imaging*, vol. 42, pp. S575–S575, SPRINGER 233 SPRING ST, NEW YORK, NY 10013 USA, 2015. pages 9
- [39] G. Stockman, S. Kopstein, and S. Benett, “Matching images to models for registration and object detection via clustering,” *IEEE Transactions on Pattern Analysis and Machine Intelligence*, no. 3, pp. 229–241, 1982. pages 9
- [40] B. Manjunath, C. Shekhar, and R. Chellappa, “A new approach to image feature detection with applications,” *Pattern Recognition*, vol. 29, no. 4, pp. 627–640, 1996. pages 9
- [41] Y. C. Hsieh, D. M. McKeown Jr, and F. P. Perlant, “Performance evaluation of scene registration and stereo matching for artographic feature extraction,” *IEEE Transactions on Pattern Analysis and Machine Intelligence*, vol. 14, no. 2, pp. 214–238, 1992. pages 9
- [42] T. W. Carrell, B. Modarai, J. R. Brown, and G. P. Penney, “Feasibility and limitations of an automated 2d-3d rigid image registration system for complex endovascular aortic procedures,” *Journal of Endovascular Therapy*, vol. 17, no. 4, pp. 527–533, 2010. pages 9, 15
- [43] X. Dai and S. Khorram, “Development of a feature-based approach to automated image registration for multitemporal and multisensor remotely sensed

- imagery,” in *Geoscience and Remote Sensing, 1997. IGARSS’97. Remote Sensing-A Scientific Vision for Sustainable Development., 1997 IEEE International*, vol. 1, pp. 243–245, IEEE, 1997. pages 9
- [44] N. Vujovic and D. Brzakovic, “Establishing the correspondence between control points in pairs of mammographic images,” *IEEE Transactions on Image Processing*, vol. 6, no. 10, pp. 1388–1399, 1997. pages 9
- [45] R. Ramli, M. Y. I. Idris, K. Hasikin, A. Karim, N. Khairiah, A. W. Abdul Wahab, I. Ahmedy, F. Ahmedy, N. A. Kadri, and H. Arof, “Feature-based retinal image registration using d-saddle feature,” *Journal of healthcare engineering*, vol. 2017, 2017. pages 9
- [46] R. W. So and A. C. Chung, “A novel learning-based dissimilarity metric for rigid and non-rigid medical image registration by using bhattacharyya distances,” *Pattern Recognition*, vol. 62, pp. 161–174, 2017. pages 10
- [47] X. Yang, R. Kwitt, M. Styner, and M. Niethammer, “Quicksilver: Fast predictive image registration—a deep learning approach,” *NeuroImage*, vol. 158, pp. 378–396, 2017. pages 10
- [48] A. Guyot, A. Varnavas, T. Carrell, and G. Penney, “Non-rigid 2d-3d registration using anisotropic error ellipsoids to account for projection uncertainties during aortic surgery,” in *International Conference on Medical Image Computing and Computer-Assisted Intervention*, pp. 179–186, Springer, 2013. pages 10, 56
- [49] A. Raheem, T. Carrell, B. Modarai, and G. Penney, “Non-rigid 2d-3d image registration for use in endovascular repair of abdominal aortic aneurysms,” in *Medical Image Understanding and Analysis*, pp. 153–157, 2010. pages 10, 56
- [50] S. Demirci, M. Baust, O. Kutter, F. Manstad-Hulaas, H.-H. Eckstein, and N. Navab, “Disocclusion-based 2d–3d registration for aortic interventions,” *Computers in biology and medicine*, vol. 43, no. 4, pp. 312–322, 2013. pages 10
- [51] M. Kerschnitzki, P. Kollmannsberger, M. Burghammer, G. N. Duda, R. Weinkamer, W. Wagermaier, and P. Fratzl, “Architecture of the osteocyte network correlates with bone material quality,” *Journal of bone and mineral research*, vol. 28, no. 8, pp. 1837–1845, 2013. pages 11, 14, 54, 58
- [52] T.-C. Lee, R. L. Kashyap, and C.-N. Chu, “Building skeleton models via 3-d medial surface axis thinning algorithms,” *CVGIP: Graphical Models and Image Processing*, vol. 56, no. 6, pp. 462–478, 1994. pages 14
- [53] G.-A. Turgeon, G. Lehmann, G. Guiraudon, M. Drangova, D. Holdsworth, and T. Peters, “2d-3d registration of coronary angiograms for cardiac procedure planning and guidance,” *Medical physics*, vol. 32, no. 12, pp. 3737–3749, 2005. pages 15

- [54] M. Groher, F. Bender, R.-T. Hoffmann, and N. Navab, “Segmentation-driven 2d-3d registration for abdominal catheter interventions,” in *International Conference on Medical Image Computing and Computer-Assisted Intervention*, pp. 527–535, Springer, 2007. pages 15
- [55] S. Gorges, E. Kerrien, M.-O. Berger, Y. Trouset, J. Pescatore, R. Anxionnat, and L. Picard, “Model of a vascular c-arm for 3d augmented fluoroscopy in interventional radiology,” in *International Conference on Medical Image Computing and Computer-Assisted Intervention*, pp. 214–222, Springer, 2005. pages 15
- [56] F. Zhou and F. De la Torre, “Factorized graph matching,” *IEEE transactions on pattern analysis and machine intelligence*, vol. 38, no. 9, pp. 1774–1789, 2016. pages 15, 55
- [57] F. Zhou and F. De la Torre, “Factorized graph matching,” in *Computer Vision and Pattern Recognition (CVPR), 2012 IEEE Conference on*, pp. 127–134, IEEE, 2012. pages 15
- [58] E. W. Dijkstra, “A note on two problems in connexion with graphs,” *Numerische mathematik*, vol. 1, no. 1, pp. 269–271, 1959. pages 23
- [59] R. A. Waltz, J. L. Morales, J. Nocedal, and D. Orban, “An interior algorithm for nonlinear optimization that combines line search and trust region steps,” *Mathematical programming*, vol. 107, no. 3, pp. 391–408, 2006. pages 32
- [60] P. E. Gill, W. Murray, and M. A. Saunders, “Snopt: An sqp algorithm for large-scale constrained optimization,” *SIAM review*, vol. 47, no. 1, pp. 99–131, 2005. pages 32
- [61] M. J. Powell, “The convergence of variable metric methods for nonlinearly constrained optimization calculations,” in *Nonlinear programming 3*, pp. 27–63, Elsevier, 1978. pages 32
- [62] F. L. Bookstein, “Principal warps: Thin-plate splines and the decomposition of deformations,” *IEEE Transactions on pattern analysis and machine intelligence*, vol. 11, no. 6, pp. 567–585, 1989. pages 32
- [63] E. Serradell, M. A. Pinheiro, R. Sznitman, J. Kybic, F. Moreno-Noguer, and P. Fua, “Non-rigid graph registration using active testing search,” *IEEE transactions on pattern analysis and machine intelligence*, vol. 37, no. 3, pp. 625–638, 2015. pages 36, 37
- [64] S. Ioffe and C. Szegedy, “Batch normalization: Accelerating deep network training by reducing internal covariate shift,” *arXiv preprint arXiv:1502.03167*, 2015. pages 59
- [65] Y. Kho and M. Garland, “Sketching mesh deformations,” in *Proceedings of the 2005 symposium on Interactive 3D graphics and games*, pp. 147–154, ACM, 2005. pages 59

Appendix

Table 2: Deformable registration results for the 20 trials of the simulated data experiments, including the 2D and 3D point-to-curve distance errors (2D/3D dist.) and the inlier ratio (IR), comparing the baseline method (ICP-TPS) and the proposed method with the shape variation between the pre-operative skeleton (P-Skeleton) and the ground truth skeleton

Trial	Method	2D dist. (pixel)		3D dist. (mm)		IR (%)
		avg.	std.	avg.	std.	
1	P-Skeleton	2.9877	-	6.0080	-	-
	ICP-TPS	0.6635	1.0009	2.1853	2.1958	60.96
	Proposed	0.0838	0.1059	0.9975	1.1403	100.00
2	P-Skeleton	4.0293	-	7.9823	-	-
	ICP-TPS	0.6926	1.0038	4.5613	5.8403	53.57
	Proposed	0.0142	0.0343	1.5044	1.6928	100.00
3	P-Skeleton	0.8423	-	1.8381	-	-
	ICP-TPS	0.5816	0.8123	1.4027	1.1917	28.79
	Proposed	0.0791	0.1043	0.5659	0.4021	100.00
4	P-Skeleton	0.8142	-	1.7706	-	-
	ICP-TPS	0.5574	0.9725	1.6106	1.6280	47.99
	Proposed	0.0899	0.0978	0.8264	0.6601	100.00
5	P-Skeleton	3.0534	-	6.0123	-	-
	ICP-TPS	0.7339	1.0830	2.4687	2.1331	50.44
	Proposed	0.1233	0.1260	1.0481	1.1010	100.00
6	P-Skeleton	1.4424	-	3.5644	-	-
	ICP-TPS	0.5224	0.9504	2.9204	3.5727	42.08
	Proposed	0.0909	0.1019	1.2686	1.4521	100.00
7	P-Skeleton	2.3928	-	4.7765	-	-
	ICP-TPS	0.3052	0.4925	1.5640	1.4539	45.25
	Proposed	0.0932	0.1130	0.9157	0.9555	100.00
8	P-Skeleton	3.7275	-	6.9198	-	-
	ICP-TPS	1.0990	1.7961	2.8101	3.1943	45.88
	Proposed	0.0824	0.0883	0.9590	1.0441	100.00
9	P-Skeleton	2.6738	-	5.3588	-	-
	ICP-TPS	0.4248	0.6425	3.9788	4.5725	54.70
	Proposed	0.0838	0.1028	1.4378	1.4960	100.00
10	P-Skeleton	0.8570	-	2.8644	-	-

	ICP-TPS	0.4616	0.5679	2.9301	3.1789	38.33
	Proposed	0.0410	0.0707	1.6225	2.0333	100.00
11	P-Skeleton	1.8527	-	3.6792	-	-
	ICP-TPS	0.6432	1.1756	3.0705	3.8758	73.91
	Proposed	0.0649	0.0992	1.3063	1.3072	100.00
12	P-Skeleton	3.0141	-	5.8035	-	-
	ICP-TPS	0.4097	0.7163	4.0634	4.6786	51.89
	Proposed	0.1421	0.1414	1.8196	1.9503	100.00
13	P-Skeleton	0.9361	-	2.0013	-	-
	ICP-TPS	0.3786	0.4663	1.7271	1.1521	52.63
	Proposed	0.0734	0.0923	0.5818	0.5234	100.00
14	P-Skeleton	2.4006	-	4.8985	-	-
	ICP-TPS	0.9758	1.3819	2.4569	2.3612	53.26
	Proposed	0.0839	0.0997	0.8845	1.1835	100.00
15	P-Skeleton	2.9285	-	5.7572	-	-
	ICP-TPS	0.6091	0.9865	3.5935	5.2652	53.13
	Proposed	0.0412	0.0553	1.2692	1.4601	100.00
16	P-Skeleton	1.3926	-	2.6105	-	-
	ICP-TPS	0.8077	1.2919	2.0426	2.1731	46.42
	Proposed	0.0851	0.0998	0.8142	0.8017	100.00
17	P-Skeleton	1.1040	-	2.3429	-	-
	ICP-TPS	0.5216	0.6201	2.2071	2.2108	59.80
	Proposed	0.1264	0.1124	1.8133	2.3430	100.00
18	P-Skeleton	3.7602	-	7.0839	-	-
	ICP-TPS	0.5634	0.8450	2.6352	3.2973	52.56
	Proposed	0.1081	0.1303	1.1361	1.6606	100.00
19	P-Skeleton	4.4739	-	8.5606	-	-
	ICP-TPS	0.7107	1.0856	4.9830	7.1273	45.20
	Proposed	0.0547	0.0861	1.6621	2.1687	100.00
20	P-Skeleton	1.5546	-	3.0297	-	-
	ICP-TPS	0.8327	1.3846	2.0439	2.8587	47.32
	Proposed	0.0725	0.0875	1.0410	1.9160	100.00

Table 3: Deformable registration results for the 20 trials of the phantom data experiments, including the 2D and 3D point-to-curve distance errors (2D/3D dist.) and the inlier ratio (IR), comparing the baseline method (ICP-TPS) and the proposed method with the shape variation between the pre-operative skeleton (P-Skeleton) and the intra-operative skeleton (ground truth)

Trial	Method	2D dist. (pixel)		3D dist. (mm)		IR (%)
		avg.	std.	avg.	std.	
1	P-Skeleton	3.7097	-	7.0949	-	-
	ICP-TPS	0.8684	1.2091	3.4822	2.8150	41.25
	Proposed	0.1278	0.1552	2.2928	1.4072	100.00
2	P-Skeleton	3.2626	-	9.7666	-	-
	ICP-TPS	0.5438	1.0683	5.7866	5.7425	45.27

	Proposed	0.1365	0.1562	2.4516	2.8172	100.00
3	P-Skeleton	1.8463	-	2.2789	-	-
	ICP-TPS	0.9360	1.4607	1.3512	1.1157	75.23
	Proposed	0.1148	0.1506	1.4733	1.4011	100.00
4	P-Skeleton	1.9586	-	2.3890	-	-
	ICP-TPS	0.6254	1.1689	1.8951	2.0478	60.96
	Proposed	0.1023	0.1421	1.4912	2.0802	100.00
5	P-Skeleton	1.3809	-	7.0198	-	-
	ICP-TPS	0.6966	1.1849	3.8378	4.2750	21.80
	Proposed	0.1103	0.1458	2.3116	2.5105	100.00
6	P-Skeleton	0.6811	-	3.9650	-	-
	ICP-TPS	0.4342	0.8481	3.6786	3.9281	78.07
	Proposed	0.1441	0.1567	2.2121	2.4100	100.00
7	P-Skeleton	1.3265	-	5.5947	-	-
	ICP-TPS	0.5070	0.7992	2.0378	1.9114	43.35
	Proposed	0.1193	0.1513	1.5134	1.3711	100.00
8	P-Skeleton	2.4982	-	7.8427	-	-
	ICP-TPS	0.7472	1.4307	3.1824	4.0426	39.42
	Proposed	0.1090	0.1464	1.5680	2.3933	100.00
9	P-Skeleton	1.1671	-	5.8493	-	-
	ICP-TPS	0.3385	0.4728	3.9999	4.7642	27.91
	Proposed	0.1037	0.1362	2.0936	2.4135	100.00
10	P-Skeleton	0.7380	-	2.9287	-	-
	ICP-TPS	0.5458	1.1293	3.3199	2.6032	60.31
	Proposed	0.1332	0.1568	2.7778	2.1949	100.00
11	P-Skeleton	1.0177	-	4.0736	-	-
	ICP-TPS	0.3790	0.5927	2.6607	3.5415	35.06
	Proposed	0.1059	0.1428	1.1592	1.2120	100.00
12	P-Skeleton	2.1920	-	6.2956	-	-
	ICP-TPS	0.7367	1.2966	3.9423	4.8153	45.86
	Proposed	0.0981	0.1389	1.3329	1.7172	100.00
13	P-Skeleton	0.9877	-	2.1023	-	-
	ICP-TPS	0.6662	1.3321	2.1678	2.7039	52.63
	Proposed	0.1072	0.1390	2.1706	2.6355	100.00
14	P-Skeleton	3.1810	-	5.1516	-	-
	ICP-TPS	1.0637	1.5387	3.0630	2.1993	54.26
	Proposed	0.1335	0.1588	2.3926	1.2918	100.00
15	P-Skeleton	2.4721	-	6.5123	-	-
	ICP-TPS	1.9178	3.5129	4.4340	4.9086	59.77
	Proposed	0.1389	0.1567	2.2874	2.4833	100.00
16	P-Skeleton	1.0649	-	2.9519	-	-
	ICP-TPS	0.7861	1.6528	2.3352	3.1259	62.91
	Proposed	0.1062	0.1434	1.4746	2.2553	100.00
17	P-Skeleton	2.1371	-	2.5390	-	-
	ICP-TPS	0.9410	1.1813	2.8399	3.3207	33.83

	Proposed	0.1131	0.1450	2.5189	2.7516	100.00
18	P-Skeleton	4.9569	-	8.1896	-	-
	ICP-TPS	0.9720	1.3656	4.0285	3.8190	55.06
	Proposed	0.1367	0.1576	2.2160	1.2725	100.00
19	P-Skeleton	4.2932	-	10.3744	-	-
	ICP-TPS	2.2838	3.8413	5.8101	6.1069	54.81
	Proposed	0.1326	0.1506	2.8411	2.8919	100.00
20	P-Skeleton	2.3853	-	3.4521	-	-
	ICP-TPS	2.3865	3.5110	2.0442	2.1804	44.69
	Proposed	0.1183	0.1493	1.7815	1.6952	100.00